Semi-Analytic Functions to Calculate the Deposition Coefficients for Ice Crystal Vapor Growth in Bin and Bulk Microphysical Models.

Jerry Y. Harrington*

Department of Meteorology and Atmospheric Science, The Pennsylvania State University, University Park, PA

G. Alexander Sokolowsky

Colorado State University

Hugh Morrison

National Center for Atmospheric Research

Corresponding author address: Department of Meteorology and Atmospheric Science, The Pennsylvania State University, University Park, PA 16802.

E-mail: jyh10@psu.edu

ABSTRACT

Numerical cloud models require estimates of the vapor growth rate for ice crystals. Current bulk and bin microphysical parameterizations generally assume that vapor growth is diffusion limited, though some parameterizations include the influence of surface attachment kinetics through a constant deposition coefficient. A parameterization for variable deposition coefficients is provided herein. The parameterization is an explicit function of the ambient ice supersaturation and temperature, and an implicit function of crystal dimensions and pressure. The parameterization is valid for variable surface types including growth by dislocations and growth by step nucleation. Deposition coefficients are predicted for the two primary growth directions of crystals, allowing for the evolution of the primary habits. Comparisons with benchmark calculations of instantaneous mass growth indicate that the parameterization is accurate to within a relative error of 1%. Parcel model simulations using Lagrangian microphysics as a benchmark indicate that the bulk parameterization captures the evolution of mass mixing ratio and fall speed with typical relative errors of less than 10%, whereas the average axis lengths can have errors of up to 20%. The bin model produces greater accuracy with relative errors often less that 10%. The deposition coefficient parameterization can be used in any bulk and bin scheme, with low error, if an equivalent volume spherical radius is provided.

1. Introduction

Numerical models of ice-containing clouds require estimates of the ice crystal vapor growth rate. However, the vapor growth rate is complex, involving the diffusion of water vapor and thermal energy through the background gas. Gas-phase diffusion, in turn, depends on the size and shape of the crystal along with the surface processes that determine the incorporation of water molecules into the crystalline lattice. It is these surface processes that control the development of crystal habits (Hallett 1965; Lamb and Scott 1972; Nelson 2001). The challenge in modeling the ice growth lies in taking simultaneous account of crystal shape effects on gas-phase diffusion along with the surface kinetic processes that influence the mass uptake of the crystal.

The most common method for parameterizing the growth and ablation of ice crystals in numerical cloud models follows the work of Houghton (1950) in using capacitance theory. Capacitance theory assumes that the vapor density is constant along the crystal surface, which occurs when the surface is rough on the nanometer scale. Surface processes are ignored in this model: facets cannot remain flat (Saito 1996, Ch. 27), and aspect ratio cannot evolve (Ham 1959) without supplementary theories (Chen and Lamb 1994). Though it was historically understood that surface processes were the drivers of the variations in habit forms, it was not clear how to include these processes in cloud models. For instance, Koenig (1971) included surface processes through a reduction factor that acts in a similar mathematical fashion to a ventilation coefficient, but this kinetic factor was not included in most subsequent models. The work of Todd (1964) and Hindman and Johnson (1972) avoided capacitance theory entirely by using laboratory-measured axis growth rates to drive habit development. Since their rate equations were taken directly from laboratory data, both surface and gas phase diffusion processes were empirically woven into the parameterization. While this line of modeling died out, it did presage current particle property approaches (Chen and

Lamb 1999; Hashino and Tripoli 2007; Chen and Tsai 2016). Most cloud model parameterizations do not include the effects of surface processes on mass uptake during vapor growth, but those that do commonly use deposition coefficients (α). Deposition coefficients account, in aggregate, for all of the surface processes occurring on the crystal surface that ultimately control the growth rates. Though all numerical models that include α treat it as a constant, this approximation is only valid over a very narrow range of conditions (Nelson 2005). In this paper, we develop a parameterization of supersaturation- and temperature-dependent α that is consistent with faceted growth and is suitable for bulk and bin microphysical models. The parameterization is developed to be flexible in that it can be used with traditional and particle property schemes. The parameterization is tested against benchmark simulations using a parcel model framework with Lagrangian bin ice microphysics, and the accuracy and limitations of the method are discussed. We first review the theory of faceted growth, and the need for a closed-form approximation for α.

2. Mass and Dimensional Growth of Faceted Ice

Deposition coefficients (α) have long been used to model the influences of surface attachment kinetic (hereafter *surface-kinetic*) processes on vapor growth (Strickland-Constable 1968). For faceted crystals, α varies explicitly with the ambient ice supersaturation (s_i, hereafter "supersaturation") and implicitly with the temperature, crystal size and shape (Nelson and Baker 1996; Wood et al. 2001). The classical theory of faceted growth posits that crystals grow primarily by the propagation of steps across their surface. In order for growth to proceed, adsorbed water molecules must attach to a step before they desorb from the surface. The fraction of molecules that adsorb, migrate to a step, and incorporate into the crystalline lattice defines the deposition coefficient.

The growth of faceted ice requires the formation of surface steps, and there are at least two mechanisms that produce them. The first mechanism is associated with natural dislocations that occur

in the crystal lattice and can outcrop on the surface. Dislocations provide permanent step sources, the theory of which originated with Burton et al. (1951). This mechanism appears to control the growth of newly formed crystals (Harrington and Pokrifka 2021) and crystals grown at low supersaturation (Nelson 2001). The second mechanism is the nucleation of two-dimensional steps on the crystal surface (step nucleation). This mechanism occurs on facets that have large defect-free areas, and appears to control the growth of larger crystals with distinct habits (Nelson and Knight 1998; Harrington et al. 2019). Indeed, Frank (1982) points out that thin crystals are only possible if steps nucleate at the crystal edge. Step nucleation is strongly dependent on the supersaturation immediately above the surface (surface supersaturation, s_{surf}), with very weak growth at s_{surf} values below some critical supersaturation, and faster growth once the critical supersaturation has been exceeded. While both theories have been developed in detail, an approximation for α that encapsulates both growth mechanisms was provided by Nelson and Baker (1996),

$$\alpha(s_{surf}, T) = \alpha_s \left[\frac{s_{surf}}{s_{char}(T)}\right]^M tanh \left[\frac{s_{char}(T)}{s_{surf}}\right]^M \quad (1)$$

where $s_{char}(T)$ is a temperature-dependent "characteristic" supersaturation that describes the supersaturation-dependence of surface-kinetic mediated growth, and M is a parameter that describes the surface growth mode. The adsorption efficiency (α_s) is thought to be near unity (Nelson 2001), which we will assume. Convenient polynomial fits to values of s_{char} derived from data (Harrington et al. 2019) are used in this study and are available from a data archive (see our data statement). A value of $M = 1$ is consistent with the theory of dislocation growth, whereas a value of $M \geq 10$ is suitable for step nucleation. In general, α rises commensurately with s_{surf}, and the rate of rise is controlled by M (Zhang and Harrington 2015, see their Fig. 1). The evidence above suggests that $M = 1$ may be appropriate for the growth of smaller crystals in numerical cloud mod-

els, whereas $M = 10$ may be more applicable to the growth of larger crystals with well-defined habits.

The above form of α has been most often used in models of faceted crystal growth requiring complex numerical solution methods (Nelson and Baker 1996; Wood et al. 2001). However, it is possible to include the above model for α in theories suitable for use in Eulerian cloud models (MacKenzie and Haynes 1992; Zhang and Harrington 2014). The theory of Zhang and Harrington (2014) combines the surface boundary conditions for faceted ice with the diffusive fluxes from the capacitance model, thus allowing for the calculation of the deposition coefficients using Eq. 1. The resulting growth equation has the same general form as the capacitance model,

$$\frac{dm}{dt} = 4\pi C(c,a)\rho_{eq} s_i D_{eff}(T,P,a,c,\alpha_a,\alpha_c), \tag{2}$$

where ρ_{eq} is the ice equilibrium vapor density, s_i is the supersaturation, $C(c,a)$ is the capacitance, and c and a are the crystal semi-dimensions that are referenced to the prism and basal faces of hexagonal ice, respectively. The combined effects of vapor and thermal energy diffusion along with surface kinetic effects (α_a and α_c) enter into the growth equation through an effective diffusivity (D_{eff}) that also depends on size and shape (see Zhang and Harrington 2014, their Eq. 15). The a- and c-axis lengths define a spheroid that is used as a surrogate for crystal shape. Spheroids are not meant to exactly represent crystal shapes, but rather to provide equations for two crystal dimensions instead of one dimension (see below).

Predicting the change in the crystal semi-dimensions (a and c) requires equations for the evolution of the axis lengths. Faceted crystals often have steps that form near crystal edges where s_{surf} is greatest, in this case the ratio of the c and a axis growth rates is (Nelson and Baker 1996),

$$\frac{dc}{da} = \frac{\alpha_c}{\alpha_a} = \Gamma \quad \text{or} \quad \frac{dln\phi}{dlnV} = \frac{\Gamma/\phi - 1}{\Gamma/\phi - 2}, \tag{3}$$

where the right-most form can be derived using the volume ($4/3\pi a^2 c$) and aspect ratio ($\phi = c/a$) of a spheroid. Current habit-evolving cloud models (Hashino and Tripoli 2007; Harrington et al. 2013) use a different form of dc/da rooted in the work of Chen and Lamb (1994), however this equation produces incorrect growth when variable deposition coefficients are used (Harrington et al. 2019). The Chen and Lamb (1994) expression is replaced with Eq. 3 in the parameterizations developed below.

Secondary habit features that appear at high supersaturations, such as dendritic branching and hollowing, cannot be modeled explicitly. These features are frequently treated through an "effective" particle density (ρ_p) that is lower than the bulk density of ice (Miller and Young 1979; Thompson et al. 2008). Chen and Lamb (1994) hypothesized that one could treat the volumetric increase in ice crystals with a deposition density (ρ_{dep}) that mimics the spatial gaps caused by branching and hollowing,

$$\frac{dV}{dt} = \frac{1}{\rho_{dep}} \frac{dm}{dt}. \tag{4}$$

The above equation, when used in combination with Eqs. 1, 2, and 3 produces crystal axis lengths, effective densities, and fall speeds that compare well to wind tunnel measurements of columnar and dendritic ice crystals grown at liquid saturation. The theory also compares well to hexagonal model solutions for crystals grown at low ice supersaturations, and to measurements of crystals grown at low pressures (Harrington et al. 2019).

While the above model provides a good approximation for faceted growth, care should be exercised when applying these theories in general. It is important to bear in mind that the surface growth mechanism can change in time. Evidence suggests that ice crystals grow by dislocations ($M = 1$) when they are relatively small and at low supersaturations. However, at higher supersaturations step nucleation ($M = 10$) is thought to control the growth since it is otherwise not possible to produce thin crystals (Frank 1982; Nelson and Knight 1998; Harrington et al. 2019), though

quasi-liquid layers (QLL) are also important (Neshyba et al. 2016; Sibley et al. 2021). Ice crystals are known to have stacking faults which reduce the nucleation barrier for surface steps (Ming et al. 1988), and Nelson and Baker (1996) have suggested modeling this growth with $M \simeq 3$ in Eq. 1. Crystals can have both slower and faster growing regions (Gonda and Yamazaki 1984), and facets can grow along the surface instead of outward (Gonda and Yamazaki 1984; Nelson and Swanson 2019). Faster growing (rough) regions can starve slower growing facets of water vapor, leading to stagnated growth rates (Harrington and Pokrifka 2021). The grain boundaries in polycrystalline ice are sources of dislocations that may cause rapid growth (Pedersen et al. 2011). Mesoscopic surface roughness has been measured on many crystals (Neshyba et al. 2013; Magee et al. 2014), but the scale of these features is generally larger than the steps that influence growth, and some of these measured crystals stop growing entirely (Magee et al. 2014). Unfortunately, measurements of many of the above growth modes are scant and theoretical models are generally lacking.

It is also important to keep in mind that spheroidal shapes are an approximation for two crystal dimensions only. It is not clear how complex crystal morphologies should be treated. For instance, it has been shown that ellipsoids are more accurate than spheroids as a representation of aggregate shapes (Jiang et al. 2019; Dunnavan et al. 2019). Complex growth morphologies, such as capped columns and the polycrystalline forms that occur at low temperatures (e.g. planar polycrystals, tetragons with side planes, scrolls, and rosettes) provide other compelling examples. These growth forms suggest that multiple axes may be needed to characterize the crystal shape, and since these crystals are faceted they can be described by faceted growth kinetics. Though predicting the precise shape of these crystals is beyond the capabilities of any current theory, it may be possible to treat the overall influence of surface kinetics on mass growth. Zhang and Harrington (2015) and Harrington et al. (2019) have shown that the overall influence of attachment kinetics on the growth of columnar and planar crystals can be treated with an equivalent volume

sphere and a particle averaged deposition coefficient. Since columnar and planar crystals have very different deposition coefficients for each crystal facet, more complex crystals may also be amenable to treatment with an average deposition coefficient. Indeed, Pokrifka et al. (2020) found that particle-average deposition coefficients characterized most of the growth of small ice crystals at temperatures below -40°C.

a. Closed-Form Approximation of the Deposition Coefficient

Calculating the deposition coefficients requires the surface supersaturation (s_{surf}) for each crystal axis (Eq. 1), however s_{surf} also depends on the gas-phase vapor diffusion rate. Consequently, s_{surf} for each crystal axis depends strongly on α (see Zhang and Harrington 2014, their Eq. 9). The problem is transcendental, requiring numerical solutions that are too costly for use in model parameterizations (Zhang 2012). It is therefore imperative to develop an approximate, yet accurate method to solve for s_{surf} in closed-form.

The strong sensitivity of α to s_{surf} is demonstrated in Fig. 1 by solving Eq. 9 of Zhang and Harrington (2014) for a planar crystal with an aspect ratio of five, and an a-axis semi-length of 86 μm that is growing by step nucleation ($M = 10$) at a temperature of -15°C and a pressure of 500 hPa. When the ambient supersaturation (s_i) is low, step nucleation is inhibited and the surface supersaturation is nearly identical to the ambient value. As the ambient supersaturation rises, growth by step nucleation commences thus keeping s_{surf} near s_{char}. The surface supersaturation rises slowly with further increases in s_i because increasing growth, through substantially rising deposition coefficients, keeps s_{surf} low. The rise in s_{surf} again becomes commensurate with s_i once α reaches unity, however, this occurs at supersaturations that are not realized in the atmosphere. The strong sensitivity of α to changes in s_{surf} indicates why a closed-form parameterization of α is difficult to achieve: Calculating the deposition coefficient requires a quantitative method to

relate s_{surf} to the ambient supersaturation for particles of any shape and size, though the equations for α are extremely sensitive to any change in s_{surf}. On the other hand, the results shown in Fig. 1 provide a hint for developing a closed-form parametrization: The variation of s_{surf} with s_i has a similar functional form for both the a- and c-axes, suggesting that a scaling law may exist that relates the two quantities. Moreover, the form of the equation for α itself (Eq. 1) suggests seeking scaling laws that exploit ratios of a measure of supersaturation with s_{char}.

Since our approach is empirical, we tested a number of different scaling relationships to calculate s_{surf}. Since s_{surf} for each axis depends on α itself, one possibility is to simply set α to unity in the equations for s_{surf} for each axis, and to scale the resulting equation with s_{char}. Rearranging Eq. 9 of Zhang and Harrington (2014) and setting α to unity for the a and c axes gives,

$$\begin{aligned} s_{diff,a} &= s_i \frac{1}{1+L_a} \qquad \text{where} \qquad L_a = \frac{ac}{C_\Delta(c,a)} \frac{\overline{v}_v}{4D_v}, \\ s_{diff,c} &= s_i \frac{1}{1+L_c} \qquad \text{where} \qquad L_c = \frac{a^2}{C_\Delta(c,a)} \frac{\overline{v}_v}{4D_v}, \end{aligned} \tag{5}$$

In the above equation, s_i is the ambient supersaturation, D_v is the vapor diffusivity in air, $\overline{v}_v$ is the mean speed of a vapor molecule, L_a and L_c are unitless quantities that depend on the crystal geometry, and $C_\Delta(c,a)$ is the capacitance evaluated one mean free path from the surface. The quantities $s_{diff,a}$ and $s_{diff,c}$ are the surface supersaturations over the a and c axes when α_a and α_c are unity, and we therefore define these as *diffusion-limited* surface supersaturations. Our empirical testing showed that, over a relatively large range of ambient supersaturations, the surface supersaturation scales with s_{char}/s_{diff} for a given axis. The form of that dependence can be well approximated with a power-law,

$$s_{surf} \sim s_{pwr} \equiv s_{diff} \left(\frac{s_{char}}{s_{diff}} \right)^{\beta} = s_{diff}^{1-\beta} \cdot s_{char}^{\beta}, \tag{6}$$

where the exponent, β, can be found by fitting to the exact calculation (Fig. 2). Simulations that we conducted indicate that the value of β is relatively insensitive to the size and aspect ratio of the

crystal. This result may be due to the inclusion of length and aspect ratio information through the variables L_a and L_c. This makes the above equations ideal for parameterization development.

The above approximation increasingly deviates from the actual surface supersaturation when approaching the low and high s_i limits, and therefore must be corrected. As s_i rises α eventually reaches unity and the surface supersaturation begins to climb away from the approximate value (a-axis in Fig. 2). As the supersaturation declines and s_{char} is approached, surface kinetics begin to dominate the growth process and s_{surf} declines rapidly, eventually becoming the same as the ambient supersaturation (blue dashed lines on Fig. 2). In order to correct the approximation for these limits, we first correct for the low supersaturation limit by taking the minimum between s_{pwr} and s_i,

$$s_{lim} = min(s_{pwr}, s_i). \tag{7}$$

This limited form of the power-law approximation deviates from the actual surface supersaturation only in the vicinity of s_{char} and at high supersaturations; these deviations are indicated by dashed circles on Fig. 2. The deviation of s_{lim} from s_{char} in these regions, which we call residuals, have consistent behavior that depends fundamentally on the ratio of s_{diff}/s_{char}, as is shown by the black lines in Fig. 3. The size and aspect ratio dependence of the residuals occurs because of the length-scales, L_a and L_c, that define s_{diff}/s_{char}. The maximum value reached by the residuals does not vary with the size or aspect ratio of the crystal (not shown). We fit the residuals as a function of the s_{diff}/s_{surf}, so that the parameterization becomes,

$$\frac{s_{diff}}{s_{surf}} \approx \frac{s_{diff}}{s_{lim}} + R_l - R_u, \tag{8}$$

where R_l and R_u are the residuals shown in Fig. 3. Note that the sign of R_l and R_u differ because the absolute value of the residual is plotted in the figure. Both residuals can be well approximated

with a similar power-law form that convolves rising and decaying functions,

$$R_l = R_{max,l}\left(\frac{s_{diff}}{s_{pwr}}\right)\left(\frac{s_i}{s_{pwr}}\right)^{p1} min\left[\left(\frac{s_i}{s_{pwr}}\right)^{p2}, 1\right],$$

$$R_u = R_{max,u}\left(\frac{s_{diff}}{s_{pwr}}\right)\left(\frac{s_{diff}}{s_{lim}}\right)^{n1}\left(max\left[0, \frac{s_{diff}}{s_{lim}} - 1\right] + 1\right)^{n2}. \quad (9)$$

The results shown in Fig. 3 indicate that the maximum in each residual curve, $R_{max,l}$ and $R_{max,u}$, is nearly constant, which we assume. The power-law exponents, $p1$, $p2$, $n1$, and $n2$, are determined by least-squares fitting. Examples of the residual fits for the a-axis of a planar crystal with an aspect ratio of 0.1 are shown by the blue dashed lines in Fig. 3. While the fit is not perfect, the small deviation from the actual curves produces very low errors in the modeled growth rates (see below). The surface supersaturation for a given axis can now be calculated approximately by rearranging Eq. 8,

$$s_{surf} \approx \frac{s_{diff}}{s_{diff}/s_{lim} + R_l - R_u}. \quad (10)$$

Each term in the above equation can be calculated based on the ambient temperature, pressure, supersaturation, and crystal axis length since the crystal geometry enters into the calculation through s_{diff}. This equation provides an approximate closed-form solution to the calculation of s_{surf} and, therefore, the deposition coefficients (Eq. 1), for each crystal axis.

An advantage of the above approach for calculating s_{surf} is that the main fitting coefficients (β, $R_{max,l}$, $R_{max,u}$, $p1$, $p2$, $n1$, and $n2$) do not depend on crystal size or geometry. However, the approximation does depend on the growth mechanism through the parameter M in Eq. 1. We therefore repeated the above fitting procedure using integer values of M ranging between unity (dislocation growth) and 15. Naturally, the fitting coefficients change substantially with different values of M, however the behavior of the coefficients themselves is regular and can be fit with up to a tenth-order polynomial in M (Fig. 4). The coefficient values for Eqs. 6 and 9, along with the

polynomial fits to the coefficients, and code to compute s_{surf} are available from a data archive (see our data statement).

b. Single-Particle Tests of the Deposition Coefficient Approximation

In order to test the accuracy of the α approximation described above, a large number of simulations were conducted against accurate benchmark calculations with the iterative solution method used by Zhang and Harrington (2014). Simulations were done for individual crystals covering a wide range of temperatures (0 to -40°C), pressures (1000 to 100 hPa), and supersaturations (near 0% to liquid saturation). We conducted simulations using initially spherical crystals with a radius of 10 μm, and the crystals grew for a time ranging from 5 to 30 minutes. In general, the approximate calculation of α produces accurate solutions to the mass and axis ratio evolution. For example, it is not possible to visually distinguish between the approximate and accurate solutions for the a and c axes of crystals grown for 10 minutes over a range of ambient supersaturations at a temperature of -15°C and a pressure of 500 hPa in Fig. 5. The level of accuracy is high regardless of whether the crystals grow by step nucleation ($M = 10$), which has a strong supersaturation dependence to the deposition coefficient, or a more efficient mechanism with $M = 3$ or $M = 1$ (dislocations). This accuracy is due entirely to the prediction of the deposition coefficients, as shown in Fig. 6. Relative errors of around 10% can occur for the minor crystal axis as α decreases with supersaturation (yellow and red curves, Fig. 6a), however these errors have only a small influence on the minor axis growth rate. The accuracy in the estimates of the deposition coefficients is due, primarily, to the accuracy in the calculation of s_{surf}, as is clearly shown in Fig. 6b using step nucleation as an example: The surface supersaturation calculated with the approximation remains near the ambient value until s_i approaches the characteristic value. At this stage, step nucleation begins and s_{surf} decreases due to vapor uptake at the crystal surface. Further increases in s_i cause

a slow rise in s_{surf} since step nucleation increases, thus increasing the vapor uptake rate and the deposition coefficient.

The aspect ratios of single crystals are strongly dependent on temperature, and the approximate model of the deposition coefficients captures this dependence (Fig. 7). These simulations show the *a*- and *c*-axis lengths and deposition coefficients after 10 minutes of growth using dislocations (M = 1) and step nucleation (M=10). Each simulation was conducted at a constant temperature (-2 to -40°C), a pressure of 500 hPa, and a relatively low supersaturation (5% of liquid saturation). A low supersaturation was used because errors are largest when the supersaturation is low. The simulations show that the crystal *a* and *c* axes after 10 minutes of growth are well captured by the approximate model for both dislocation and step nucleation growth. Small deviations (relative errors less than 6%) appear in the axis lengths after 10 minutes of growth when step nucleation growth is assumed. The approximate model also captures the cessation of axis growth when s_{surf} falls substantially below s_{char} for a given axis length (at temperatures below -12.5°C for the c-axis and below -19°C for the a-axis). Indeed, at temperatures below -20°C crystal growth is effectively suppressed at the supersaturations used in these calculations, since the s_{char} are substantially larger than s_{surf} (not shown). Note that the cessation of dimensional growth has been observed in the laboratory (Nelson and Knight 1998; Magee et al. 2014) and may be responsible for extremely thin crystals that are sometimes observed (Jensen et al. 2008). The errors shown in these calculations are representative of the approximate form of s_{surf} across a wide range of temperatures, pressures, and supersaturations. In order to illustrate the degree to which attachment kinetics affect the growth rates, calculations using the Chen and Lamb (1994) adaptive-habit method are also shown. The adaptive habit method assumes that growth is diffusion-limited, leading to much stronger growth of the a- and c-axes, and to generally thinner crystals.

3. Deposition Coefficient Parameterization

Given the accuracy of the approximate form of α, we next develop parameterizations for bin and bulk microphysical models. Eulerian bin microphysical parameterization is relatively straightforward given that bin widths are narrow enough to perform deposition coefficient calculations using the bin-average crystal dimensions. Bulk parameterization requires a different approach since the growth rates are integrated analytically across a wide range of crystal dimensions. We discuss each parameterization in turn and then describe tests of the parameterizations against a Lagrangian bin microphysical model.

a. Bin Microphysical Model Parameterization

Eulerian bin microphysical modeling is computationally costly, but has the advantage that no assumptions are made about the shape of the size distribution. However, Eulerian bin models do suffer from numerical problems such as artificial distribution broadening caused by numerical diffusion on the Eulerian mass grid, and on the spatial grid in Eulerian cloud models (Morrison et al. 2018) though this latter effect appears to be small in some cases (Pardo et al. 2020). The Eulerian bin microphysical framework from our prior work (e.g. Harrington et al. 1999) is expanded here to use variable deposition coefficients, and to predict two axis lengths and an effective density consistent with the approach of Harrington et al. (2013). The bin model uses the method-of-moments approach for mixed-phase microphysics (Reisin et al. 1996) and predicts the number and mass mixing ratio for each of 35 Eulerian size bins, with bin edges defined by mass doubling. The 35 bins span an equivalent volume diameter range of 3 to 4030 μm, which is sufficient for the growth processes modeled here.

The transport of number and mass mixing ratio among bins is treated in a semi-Lagrangian sense following the "top-hat" method advocated by Stevens et al. (1996). The top-hat method

for growth and the remapping of the particle properties among bins assumes that the distribution is flat within a bin (Fig. 8). The lower and upper mass edges ($m_l(t)$ and $m_u(t)$, respectively) of the top-hat are defined following the procedure in Stevens et al. (1996), and the new mass edges at the end of a time-step ($m_l(t+\Delta t)$ and $m_u(t+\Delta t)$) are determined from the solution to the growth equation. Though the capacitance and the deposition coefficients vary with the crystal dimensions, the growth equation can be integrated forward in time with relatively low error using some simplifying approximations (Chen 1992; Harrington et al. 2019): If the time-step is less than about 20 seconds, Eq. 2 can be integrated assuming an equivalent volume sphere (radius r_{eq}) with the shape factor ($q_{eq} = C(a,c)/r_{eq}$), particle effective density (ρ_p), and the effective diffusivity (D_{eff}) assumed constant over the time-step (Δt),

$$m(t+\Delta t) = \left[m(t)^{2/3} + \frac{8\ \pi\ \alpha_v\ q_{eq}\ D_{eff}\ \rho_{eq}\ \overline{s_i}\ \Delta t}{3\ \rho_p^{1/3}} \right]^{3/2}, \tag{11}$$

where $\alpha_v = [3/(4\pi)]^{1/3}$ originates from the definition of the equivalent volume spherical mass ($m = 4/3\pi r_{eq}^3 \rho_p$). The deposition coefficients are computed using the average a- and c-axes for a given bin. This equation (Eq. 11) is similar to Eq. A2 in Stevens et al. (1996) except that the integral forcing term τ is written as the time-step averaged supersaturation, $\overline{s_i}$. The time-step averaged supersaturation is computed from the supersaturation forcing equation following Wu (1999). The method is the same as that of Stevens et al. (1996) and mass closure is enforced (Tzivion et al. 1989), thus ensuring mass conservation.

Equation 11 is used to evolve the top-hat mass edges in time, and remap distribution properties among the bins. In the example shown in Fig. 8, the resulting growth causes the top-hat distribution to straddle two bins. The number concentration within bin-k (N_k) is redistributed based on the fractional area of the top-hat that resides within a given bin while preserving the total concentra-

tion,

$$N_k = \frac{1}{\Delta m}\int_{m_l}^{m_u} N_k dm = \frac{1}{\Delta m}\int_{m_l}^{m_{k+1}} N_k dm + \frac{1}{\Delta m}\int_{m_{k+1}}^{m_u} N_k dm = N_k \frac{m_{k+1}-m_l}{\Delta m} + N_k \frac{m_u - m_{k+1}}{\Delta m}, \quad (12)$$

where $\Delta m = m_u - m_l$ and m_u and m_l are the values at the end of the time-step. The right-most term in the equation above represents the concentration that is remapped to the next bin (shown as the blue shaded region in Fig. 8) whereas the left-most term represents the concentration that remains in the original bin (unshaded region). This approach is also applied to the mass moment, thus conserving mass during vapor growth.

Predicting a second axis length and effective density requires transporting information on aspect ratio and volume as well as number and mass. Jensen et al. (2017) showed that aspect ratio and effective density can be tracked accurately on the spatial grid of an Eulerian cloud model if mixing ratios of total volume and total volume times aspect ratio are conserved. We follow this approach here and conserve the moments,

$$\begin{aligned} V_k &= \frac{1}{\Delta m}\int_{m_l}^{m_u} N_k V dm \simeq \frac{1}{\overline{\rho_p}\Delta m}\int_{m_l}^{m_u} N_k\, m\, dm \\ \Phi_k &= \frac{1}{\Delta m}\int_{m_l}^{m_u} N_k V \phi dm \simeq \frac{\overline{\phi}}{\overline{\rho_p}\Delta m}\int_{m_l}^{m_u} N_k\, m\, dm \end{aligned} \quad (13)$$

where V_k and Φ_k are the total volume and total volume times aspect ratio in bin-k. General analytical expressions for the co-variation of the effective density and aspect ratio with size do not exist, and we therefore use bin-averaged quantities ($\overline{\rho_p}$ and $\overline{\phi}$). This approximation allows us to write the volume as $V = m/\overline{\rho_p}$, and therefore the above moment equations reduce to variations of the mass-moment, which are shown as the right-most equations (Eq. 13). This approach is attractive because the mass-moment remapping can be used for V_k and Φ_k, however it requires estimates of $\overline{\rho_p}$ and $\overline{\phi}$ at the end of a time-step.

There are several procedures that could be invoked to estimate $\overline{\rho_p}$ and $\overline{\phi}$, and each approach has its limitations. However, testing shows that the following approach is most accurate. Since

the change in mass is known, we calculate the volume of the upper (V_u) and lower (V_l) top-hat mass edges at the end of a time-step using Eq. 4. We then estimate the new particle density by preserving the zeroth moment, $\int_{m_l}^{m_u} N_k dm = \int_{V_l}^{V_u} N_k \overline{\rho_p} dV$ which implies that

$$\overline{\rho_p} = \frac{m_u - m_l}{V_u - V_l}. \tag{14}$$

This method produces average effective densities that are higher than Lagrangian bin microphysical calculations (see §4 below). However, it provides a better overall match with the ice water content, axis lengths, and fall-speed, quantities that are arguably more critical to capture accurately. Finally, we can use the change in the average volume to estimate the change in the average aspect ratio directly from Eq. 3 by assuming that the ratio Γ/ϕ is constant over a typical time-step (less than 20 s), which is usually a good approximation.

b. Bulk Microphysical Model Parameterization

Treating variable deposition coefficients in a bulk microphysical model is less straightforward, since the deposition coefficients vary considerably across the size distribution. Nevertheless, our prior work shows that it is possible to accurately parameterize the influences of constant deposition coefficients (Harrington et al. 2009). In this section, we use this approach to extend the adaptive habit parameterization of Harrington et al. (2013) and Jensen et al. (2017) so that it is consistent with variable deposition coefficients. We also provide an approach for the general use of variable deposition coefficients in any bulk model.

Including variable deposition coefficients in a bulk model ultimately involves approximating the integrated mass growth rate, which gives the change in the ice mixing ratio (q_i) in time,

$$\frac{dq_i}{dt} = \frac{1}{\rho_a} \int_0^\infty \frac{dm(a)}{dt} n(a) da \tag{15}$$

where ρ_a is the air density, the mass is a function of a length-scale (a), and $n(a)$ is the gamma distribution. The length scale we use here is the a-axis length of a spheroid as defined in Harrington et al. (2013). This integral cannot be solved analytically for variable deposition coefficients because the effective diffusivity (D_{eff}) varies with size. Harrington et al. (2009) showed that when the deposition coefficient is constant, the above integral can be approximated accurately if D_{eff} is calculated at an appropriate "kinetic" length-scale. Zhang (2012) showed that this approach can be extended to variable deposition coefficients if the ratio of the second and first moments of the distribution are used to define the kinetic length scales for the a- and c-axes,

$$a_{kin} \equiv \frac{\int_0^\infty a^2 n(a) da}{\int_0^\infty a n(a) da} = a_n \frac{\Gamma(\nu+2)}{\Gamma(\nu+1)} \quad \text{and} \quad c_{kin} \equiv c_n \frac{\Gamma(\nu+2)}{\Gamma(\nu+1)}. \tag{16}$$

In the above equation, ν is the distribution shape and the characteristic length scale a_n is used in the gamma distribution definition. Both a_n and c_n are directly related to the number-weighted mean a- and c-axis lengths (for details see Harrington et al. 2013). The kinetic length-scales are used to calculate representative values of the deposition coefficients ($\overline{\alpha_a}$ and $\overline{\alpha_c}$), which are then used to calculate a representative value of $\overline{D}_{eff} \equiv D_{eff}(\overline{\alpha_a}, \overline{\alpha_c}, a_{kin}, c_{kin}, T, P)$. When these approximations are used in Eq. 2 they allow us to write Eq. 15 as,

$$\frac{dq_i}{dt} \simeq \frac{N_i}{\rho_a} 4\pi \, \overline{C} \, \overline{D_{eff}} \, \rho_{eq} \, s_i, \tag{17}$$

where N_i is the ice concentration and $\overline{C}$ is the distribution-averaged capacitance. The above equation allows us to calculate changes in ice mass mixing ratio subject to the influences of variable deposition coefficients, and it should be generally applicable since the form is nearly identical to that used in most bulk microphysical schemes. In addition to using $\overline{\alpha_a}$ and $\overline{\alpha_c}$ in D_{eff} to estimate the overall effects of surface kinetics on mass growth, we also use these values in Eq. 3 to evolve the average a- and c-axis lengths following the procedure in Harrington et al. (2013). These modifications make the bulk adaptive habit microphysical model (Harrington et al. 2013; Jensen et al.

2017) consistent with faceted growth and variable deposition coefficients. In the next section, both the Eulerian bin and bulk habit models are tested against Lagrangian bin microphysics.

4. Parcel Model Testing against Lagrangian Microphysics

The parameterizations are implemented into a parcel model framework (Sulia and Harrington 2011) and are tested against a Lagrangian bin microphysical model that includes variable deposition coefficients (Zhang and Harrington 2015). Parcel models are idealized in that only parcel lifting at either a constant or sinusoidally varying updraft speed is used to provide the supersaturation forcing. No mixing with the environment occurs, and all of the hydrometeors move with the parcel. However, the idealized nature of parcel models makes them useful for testing microphysical schemes since complicating processes (such as mixing and sedimentation) are ignored. The influence of growth processes alone can therefore be isolated, and biases and errors are easier to detect. The parcel model used here (described fully in Zhang and Harrington 2015) solves differential equations for the temperature, pressure, height, and total water mixing ratio, along with the microphysical equations. The Lagrangian bin microphysics is configured with 100 ice crystal bins for which the a- and c-axes, mass, and effective density are tracked. Since the growth of each bin is followed explicitly, the Lagrangian model results are used as the benchmark against which the Eulerian bin and bulk solutions are tested. The parcel model in each case is run for 4000 seconds and initialized with a constant updraft speed, initial temperature, and initial pressure that varies for each simulation (described below). The initial relative humidity with respect to liquid for all simulations is 0.95, and this allows us to explore diffusion and kinetics-limited growth in a single simulation: High supersaturations and α are produced early in the simulations, whereas low supersaturations and α occur later in the simulations. Liquid water is not included in the simulations and ice is nucleated instantaneously at the first time-step, which removes complications

that mixed-phase processes and nucleation feedbacks introduce. The instantaneously nucleated ice is spherical with an average initial radius of 10 μm for all the models. This initial ice spectrum is distributed over the the bins of the Lagrangian and Eulerian models during the first time-step using a gamma distribution with a shape of $\nu = 4$. Note that the results are not highly sensitive to the assumed shape of the initial ice spectrum. A distribution shape of $\nu = 5$ is prescribed for the bulk model because this value produces the best match with the Lagrangian simulations, and therefore provides an estimate of the minimum error associated with the parameterization. Deposition coefficients in all models are predicted with the parameterization described above using step nucleation ($M = 10$) for two reasons: First, the development of crystal habits is thought to be due to step-nucleation mediated growth (Frank 1982). Second, step nucleation is the most error-prone growth process to model due to the strong supersaturation dependence of α.

Parcel model simulations were conducted for a range of constant vertical motions (from 0.1 to 1 m s^{-1}), a range of initial temperatures from -4 to -45 °C, and a range of ice concentrations from 10 to 500 L^{-1}. Vertical motion primarily alters the supersaturation forcing term, and since errors tended to be somewhat larger at lower vertical motions we only show results for a fixed vertical motion of 0.25 m s^{-1}. In the analyses presented below, we first provide time-series results from a selected set of simulations that are representative of the ensemble of simulations. These results are followed by analyses of simulation-averaged results over a range of initial temperatures, which provide a broader picture of the parameterization accuracy.

a. Time-series Results

Time-series results for two sets of simulations conducted at high (-15°C and 850 hPa) and low (-45°C and 300 hPa) respective initial temperatures and pressures are shown in Fig. 9. For these simulations, s_{char} and ρ_{dep} were held constant at their initial values so that temperature feedbacks

to the growth through α and the density do not occur. Consequently, any errors that appear should be due primarily to the evolution of the particle axis lengths. The constancy of s_{char} and ρ_{dep} is relaxed in the next subsection.

For all of the simulations (Fig. 9a), the supersaturation rises and then declines depending on when ice crystal growth dominates over the supersaturation production caused by vertical lifting. At -15°C and a concentration of 10 L^{-1} the supersaturation rises above that of liquid, but as noted above we have neglected liquid-phase microphysics. Note that both the Eulerian bin and the bulk microphysical schemes capture the supersaturation evolution, though it is over-estimated in the bulk model, and under-estimated in the Eulerian bin model. This result illustrates the reason we ignored liquid-phase microphysics for these simulations: Not only does liquid-phase microphysics introduce another complicating process, but liquid-phase microphysics would limit the supersaturation rise and therefore may not expose differences in model performance. Note that the supersaturation predicted by the Eulerian bin model is nearly identical to the Lagrangian solution at the higher ice concentration, however the bulk model prediction remains slightly high.

The ice water content (Fig. 9b) rises continuously with time, but begins to asymptote as the supersaturation approaches steady-state. This is well predicted by both the Eulerian bin and the bulk models, though there are small differences that are difficult to discern in the figure: Since the bulk model over-predicts the supersaturation, it tends to slightly under-predict the ice water content (since total mass is conserved). The semi-axis lengths averaged over the size distributions (Fig. 9c and d) are consistent with the behavior expected at each temperature. At -15°C the average major semi-axis length (a-axis) increases rapidly reaching nearly 800 μm when the concentration is low (10 L^{-1}) whereas the minor semi-axis (c-axis) remains small. This growth is consistent with planar dendrites, and it is dependent on the ice concentration. The reason for the concentration dependence is the lack of a liquid phase: Including a liquid-phase would keep the

supersaturation near that of liquid saturation, thus constraining the growth and limiting the ice concentration dependence. At -45°C columnar crystals are produced with much smaller major semi-axis dimensions (up to 150 μm) than crystals grown at the higher temperature. The Eulerian bin and bulk models capture the evolution of the average major semi-axis length with relatively high accuracy. The average minor semi-axis, in contrast, is only well-predicted by the Eulerian bin model. The bulk microphysical model either over- or under-predicts this axis length by 14% at -15°C and 30% at -45°C.

While the distribution shape is fixed in the bulk microphysical model, it varies with time in the Eulerian and Lagrangian bin models. The Lagrangian bin model produces a rapid narrowing of the crystal size spectrum (Fig. 10), an expected result that Sheridan et al. (2009) showed is due to the faster habit development and growth of initially smaller particles. The Eulerian bin model captures the evolution of the distributions for both axis lengths in that the distribution mode is relatively well predicted. The a-axis distribution appreciably narrows similarly to the Lagrangian model, however the c-axis distribution width remains broader and is skewed towards the lower end. This result is due to the use of an average aspect ratio for each bin.

The Eulerian bin and bulk microphysical models approximate the manner in which the deposition coefficients, the effective density, and the aspect ratio are treated during growth, and some variables will thus be predicted with lower precision, a consequence that is clearly shown in Fig. 11. The effective density is relatively well predicted by the bulk microphysical model at -15°C, however it is slightly under-predicted at -45°C. It is possible to produce a better prediction of the density at lower temperature, but doing so causes the fall speed error to become greater than the 28% relative error shown in Fig. 11c. In contrast, the average effective density predicted by the Eulerian bin model is generally too high, though the fall speeds are predicted with a relative error of less than 10%. It is possible to predict the density more accurately by using mass moment con-

servation instead of the zeroth moment (Eq. 14). However, doing so leads to particles with smaller a- and c-axis lengths, and fall speeds that are much lower and with larger error (over 20%). The key point is that improving the prediction of one variable will necessarily introduce errors in other variables, and we choose to minimize the error in the ice water content and fall speed. It is also worth noting that the accuracy of the Eulerian bin parameterization is not strongly dependent on bin resolution. Tests with bin spacing reduced by half and one quarter produced nearly indistinguishable results, and so they are not included on the figures. The insensitivity to bin resolution is due to a few factors. First of all, mass doubling is used to define the bin edges, and this leads to increasing bin widths for larger crystals. Therefore, reducing the bin width has less of an effect at larger sizes. Larger crystals also have the lowest densities, and accurate predictions of both aspect ratio and density are difficult to achieve when an average density is estimated for each bin. The relative insensitivity of the parameterization to bin width is a disadvantage, in that higher accuracy cannot be attained by reasonable refinements to the bin width. However, it is also an advantage in that using smaller numbers of bins will not strongly decrease the accuracy of the scheme.

In contrast to the effective density and the fall speed, the distribution-averaged deposition coefficients are relatively well predicted by each model. The deposition coefficient for the major semi-axis is always greatest, and this is expected: The surface supersaturation maximizes near regions of high curvature, such as at narrow end of a plate or a column, thus leading to larger α. Note that α for the major semi-axis begins above 0.1 when the supersaturation is high. Values of α above about 0.1 do not cause strong reductions in mass growth (Gierens et al. 2003). Growth of the major axis is therefore not strongly inhibited by surface kinetics early in the simulations, and is driven primarily by gas-phase diffusion. In contrast, the deposition coefficient for the minor axis is always below 0.1. The minor axis is therefore strongly inhibited by surface kinetics, and this is the reason that the modeled crystals develop planar and columnar shapes over time. As the simulations

progress, the supersaturation in each case declines and α for the major axis even decreases below 0.1 indicating that growth is increasingly inhibited by surface processes. The bulk and Eulerian bin models capture these transitions remarkably well, especially given the strong supersaturation dependence of step nucleation.

b. Simulation-Averaged Results

The above time-series results are illuminating, but a broader picture of the parameterization results can be painted if we examine the various microphysical quantities, both averaged over the course of the simulations and as a function of the initial temperature. In the simulations presented below, we relax the assumption that the deposition density and the characteristic supersaturations are fixed at their initial value. Simulations are shown for initial temperatures between -4 and -40°C, a pressure of 850 hPa, and for three initial ice concentrations of 10, 50, and 500 L^{-1}, which produces a wide range of average particle sizes and aspect ratios.

The simulation results show that both the Eulerian bin and bulk models predict the average ice water content trend with temperature, and with small relative errors (less than 5%) at all concentrations and at initial temperatures below -10°C (Fig. 12a). The ice water content decreases commensurately with temperature, as expected. Note that all the models predict a local minimum in the predicted ice water content near -9°C at lower ice concentrations (N_i = 10 L^{-1}). The minimum in ice water content is due to the isometric growth of the crystals near -9°C, which is much slower than the columnar and planar growth that occur near -6 and -15°C, respectively (Sulia and Harrington 2011). This result indicates that the Eulerian bin and bulk parameterizations can capture an important feature of habit-dependent growth, even though the relative error in the ice water content is larger at higher temperatures: At initial temperatures above -10°C the relative error reaches values of up to 14%.

The Eulerian bin and the bulk models also capture the general temperature dependence of the a- and c-axes of the crystals (Fig. 12c and d), with planar dendritic crystals that have low effective density (Fig. 12b) predicted between temperatures of -10 and -20°C, and columnar crystals predicted at temperatures above -10°C. The effective density is well predicted by the bulk model at temperatures above -20°C, however the Eulerian bin model tends to over-predict the effective density. These results are consistent with those of the last section, and while we could alter the model to improve the effective density, the accuracy of the ice water content and the fall speed prediction (Fig.13b) would then suffer. Though it is difficult to discern from the figure, the simulated crystals are isometric at temperatures below -30°C with relatively high effective density. As pointed out in Harrington et al. (2019), little data on s_{char} exist at temperatures below -30°C, and crystals at these temperatures are often polycrystalline. Given our limited knowledge we used a single s_{char} for growth at low temperatures, leading to isometric crystals. Modeling either planar or columnar growth at low temperatures, as was done in the subsection above, requires reducing s_{char} for the major axis, though little data is available to guide such a choice.

The Eulerian bin model predicts the average axis evolution with a high degree of accuracy in that relative errors are less than 2%. In contrast, the bulk microphysical model tends to under-predict both average axis lengths by up to 20%. The larger error in the axis lengths is due primarily to the constant distribution shape, ν, which fixes the spectrum with a greater breadth than that simulated by the Lagrangian and Eulerian bin models. It is possible to improve upon the accuracy with which the bulk average axis lengths are predicted by changing the distribution shape. For instance, Fig. 13a shows that distribution shapes ranging between 3 and 6 produce average axis lengths that encompass the Lagrangian model solutions. However, using much smaller or larger values of ν then increase errors in other quantities including the ice water content (not shown) and fall speed (Fig. 13b). For instance, a value of $\nu = 6$ produces larger average axis lengths, which

causes much larger fall speeds. However, at $T <$ -20°C, a smaller value of ν=3 also produces larger fall speeds even though the crystal sizes are smaller. This result is due to the increase in the effective density that occurs as ν is reduced (not shown). A ν value of 5 appears to produce the best prediction of both the ice water content and the fall speed as compared to the Lagrangian bin model. However, it is worth keeping in mind that these benchmark comparisons do not include processes that will naturally broaden the size spectrum, such as differential vertical advection due to sedimentation, mixing, aggregation, and ice nucleation. One could therefore argue that a smaller value of ν may be more appropriate for simulations in Eulerian cloud models.

The deposition coefficient parameterization developed above is general enough for use in any bulk microphysical scheme. Harrington et al. (2019) have shown that accurate mass growth rate calculations are possible if the growth rate is evaluated using the equivalent volume spherical radius (r_{eq}) and an average characteristic supersaturation ($\overline{s}_{char}$),

$$\frac{dq_i}{dt} \simeq \frac{N_i}{\rho_a}\, 4\pi\, \overline{r_{eq}}\, q_{eq}\, \overline{D_{eff}}[\alpha(\overline{s}_{char}), r_{eq}]\, \rho_{eq}\, s_i, \tag{18}$$

where $q_{eq} = \overline{C}/r_{eq}$ is an effective shape factor, and $\overline{D_{eff}}[\alpha(\overline{s}_{char}), r_{eq}]$ is the effective diffusivity evaluated at r_{eq} using a single α calculated with the average value of s_{char}. In order to test the accuracy of this approximation for bulk models, the simulations shown in Fig. 12 were recomputed using Eq. 18 to calculate the mass growth only. Crystal shapes were still allowed to develop in time using the $\overline{\alpha}_a$ and $\overline{\alpha}_c$ values for each axis. Since the evolution of the crystal a- and c-axes is tied to changes in volume through the mass growth rate (see Eq. B26, Harrington et al. 2013), the change in crystal mass evolution will be consistent with Eq. 18. Consequently, any errors in the approximate mass growth rate should appear in the evolution of the crystal shapes and the ice water content, however, the relative errors in those quantities was always below 1%. To illustrate the low relative errors, Fig. 14 shows the simulation-averaged ice water content growth rate as a

function of the initial temperature. The overall mass uptake rate from the bulk model that uses a single α (Eq. 18) is nearly identical to the model that predicts both α_a and α_c. Note that the α value calculated with the above approach falls between α_a and α_c. The value of α tends to reside nearest the value for the fastest growing axis, and this makes physical sense: During either planar or columnar growth the major axis dominates the overall mass uptake by the crystals, and thus α for this axis will control most of the growth. These results indicate that Eq. 18 provides a useful approximation of the supersaturation-dependent deposition coefficient for bulk microphysical schemes.

5. Summary and Concluding Remarks

Surface attachment kinetics are often treated in numerical cloud models with a constant deposition coefficient. Such an approximation is only valid for a small range of conditions, and it is inappropriate for faceted crystals, including crystals with small faceted structures such as dendrites and the lacunae that occur with hollowed columns and plates. While theories for supersaturation-dependent deposition coefficients consistent with the growth of faceted ice have been available for many years, methods to connect those theories to the growth equations used in cloud models have been lacking. Moreover, the numerical procedures needed to calculate the deposition coefficients consistently with the equations for vapor growth are cumbersome and computationally costly. In this work, we provide an efficient method for calculating the deposition coefficient. This approximate method produces small errors (less than 1%) relative to benchmark numerical solutions and allows for the specification of different surface growth modes, therefore providing flexibility in calculating α.

The approximate method for calculating the deposition coefficient was parameterized for Eulerian bin and bulk microphysical models by making use of prior modeling methods. Parcel

tests of the Eulerian bin and bulk schemes indicate that both models are capable of reproducing temperature-dependent habit growth at low and high supersaturations, including the development of low density planar crystals consistent with dendrites, and narrow columnar crystals consistent with needles and hollow columns. Moreover, temperature-dependent features of the ice water content, such as a minimum near a temperature of -9°C, are reproduced by both bin and bulk models. The ice water content is generally simulated with relatively low error by both models, though errors can reach 14% at higher temperatures (above -6°C). Fall speeds and average axis lengths are well predicted by the Eulerian bin model (relative errors $< 10\%$), however effective density is over-predicted. In contrast, the bulk model predicts the effective density with lower relative error, but produces larger errors in the average axis lengths (up to 20%). Better axis length prediction by the bulk model is possible by changing the distribution shape parameter (ν), however doing so can produce larger errors in the fall speed (over 20%). Using an equivalent volume radius sphere and a single deposition coefficient can reproduce the growth rates of highly anisotropic crystals, and therefore provides a method for including variable deposition coefficients in any bulk scheme. It is worth noting that the present parameterization is perhaps most easily adapted to Lagrangian super-particle schemes, where the properties of particles are tracked in a Lagrangian sense within an Eulerian spatial framework (e.g. Shima et al. 2020)

Even though our focus is on ice crystal growth, for completeness we point out that sublimating crystals can also be treated with the framework described in this manuscript, though with modifications. Sublimation causes the crystal surface to roughen rapidly (Magee et al. 2014), and the sublimation coefficient appears to be near unity (Magee et al. 2011). Moreover, single crystals become spheroidal during sublimation, and their aspect ratios remain approximately constant (Nelson 1998).

Acknowledgments. The authors are grateful for support from the National Science Foundation under Grant #AGS-1824243 and for support from the U.S.Department of Energy's Atmospheric Science Program Atmospheric System Research, an Office of Science, Office of Biological and Environmental Research program under Grants DE-SC0012827 and DE-SC0021001. Three anonymous reviewers are thanked for their time and effort, and comments that improved the contents of this manuscript.

Data Statement: Data tables for the fits to the surface supersaturation, and output from from the calculations used to produce the figures are available from The Pennsylvania State University Data Commons at https://doi.org/10.26208/f6q0-8p03. Fortran codes to calculate the characteristic and surface supersaturation, and the deposition coefficients is also available through Data Commons at https://doi.org/10.26208/s7de-et44.

References

Burton, W. K., N. Cabrera, and F. C. Frank, 1951: The growth of crystals and the equilibrium structure of their surfaces. *Philosophical Transactions of the Royal Society of London. Series A, Mathematical and Physical Sciences*, **243 (866)**, 299–358.

Chen, J.-P., 1992: Numerical Simulation of the Redistribution of Atmospheric Trace Chemicals Through Cloud Processes. Ph.D. thesis, The Pennsylvania State University, University Park, PA, 16802, 342pp.

Chen, J.-P., and D. Lamb, 1994: The theoretical basis for the parameterization of ice crystal habits: Growth by vapor deposition. *J. Atmos. Sci.*, **51**, 1206–1221.

Chen, J.-P., and D. Lamb, 1999: Simulation of cloud microphysical and chemical processes using a multicomponent framework. Part II: Microphysical evolution of a wintertime orographic cloud.

675 *J. Atmos. Sci.*, **56**, 2293–2312.

676 Chen, J.-P., and T.-C. Tsai, 2016: Triple-moment modal parameterization for the adaptive growth
677 habit of pristine ice crystals. *J. Atmos. Sci.*, **73**, 2105–2122.

678 Dunnavan, E. L., Z. Jiang, J. Harrington, J. Verlinde, K. Fitch, and T. Garrett, 2019: The shape
679 and density evolution of snow aggregates. *J. Atmos. Sci.*, **76**, 3919–3940.

680 Frank, F. C., 1982: Snow crystals. *Contemporary Physics*, **23 (1)**, 3–22, doi:10.1080/
681 00107518208231565.

682 Gierens, K., M. Monier, and J.-F. Gayet, 2003: The deposition coefficient and its role for cirrus. *J.*
683 *Geophys. Res.*, **108(D2)**, 4069.

684 Gonda, T., and T. Yamazaki, 1984: Initial growth forms of snow crystals growing from frozen
685 cloud droplets. *J. Meteorol. Soc. Japan*, **62**, 190–192.

686 Hallett, J., 1965: Field and laboratory observations of ice crystal growth from the vapor. *J. Atmos.*
687 *Sci.*, **22**, 64–69.

688 Ham, F., 1959: Shape-preserving solutions of the time-dependent diffusion equation. *Quarterly of*
689 *Applied Mathematics*, **17**, 137–145.

690 Harrington, J., and G. Pokrifka, 2021: Approximate models for lateral growth on ice crystal sur-
691 faces during vapor depositional growth. *J. Atmos. Sci.*, Early Online Release.

692 Harrington, J., K. Sulia, and H. Morrison, 2013: A method for adaptive habit prediction in bulk
693 microphysical models. Part I: Theoretical development. *J. Atmos. Sci.*, **70**, 349–364, doi:10.
694 1175/JAS-D-12-040.1.

Harrington, J. Y., R. Carver, and D. Lamb, 2009: Parameterization of surface kinetic effects for bulk microphysical models: Influences on simulated cirrus dynamics and structure. *J. Geophys. Res.*, **114**, D06 212.

Harrington, J. Y., A. Moyle, L. E. Hanson, and H. Morrison, 2019: On calculating deposition coefficients and aspect-ratio evolution in approximate models of ice crystal vapor growth. *Journal of the Atmospheric Sciences*, **76 (6)**, 1609–1625, doi:10.1175/JAS-D-18-0319.1.

Harrington, J. Y., T. Reisin, W. R. Cotton, and S. M. Kreidenweis, 1999: Cloud resolving simulations of Arctic stratus. Part II: Transition-season clouds. *Atmos. Res.*, **51**, 45–75.

Hashino, T., and G. J. Tripoli, 2007: The spectral ice habit prediction system (SHIPS). Part I: Model description and simulation of the vapor deposition process. *J. Atmos. Sci.*, **64**, 2210–2237.

Hindman, E. E., and D. B. Johnson, 1972: Numerical simulation of ice particle growth in a cloud of supercooled water droplets. *J. Atmos. Sci.*, **29**, 1313–1321.

Houghton, H. G., 1950: A preliminary quantitative analysis of precipitation mechanisms. *J. Atmos. Sci.*, **7**, 363–369.

Jensen, A., J. Harrington, H. Morrison, and J. Milbrandt, 2017: Predicting ice shape evolution in a bulk microphysics model. *J. Atmos. Sci.*, **74**, 2081–2104.

Jensen, E., and Coauthors, 2008: Formation of large ($\sim$ 100 micron) ice crystals near the tropical tropopause. *Atmospheric Chemistry and Physics*, **8 (6)**, 1621–1633.

Jiang, Z., J. Verlinde, E. Clothiaux, K. Aydin, and C. Schmitt, 2019: Shapes and fall orientations of ice particle aggregates. *J. Atmos. Sci.*, **76**, 1903–1916.

Koenig, L., 1971: Numerical modeling of ice deposition. *J. Atmos. Sci.*, **28**, 226–237.

Lamb, D., and W. Scott, 1972: Linear growth rates of ice crystals grown from the vapor phase. *J. Crystal Growth*, **12**, 21–31.

MacKenzie, A., and P. Haynes, 1992: The influence of surface kinetics on the growth of stratospheric ice crystals. *J. Geophys. Res.*, **97**, 8057–8064.

Magee, N., A. Miller, M. Amaral, and A. Cumiskey, 2014: Mesoscopic surface roughness of ice crystals pervasive across a wind range of ice crystal conditions. *Atmos. Chem. Phys.*, **14**, 12 357–12 371.

Magee, N., K. Spector, Y.-H. Lin, C. Tong, and J. BEATTY, 2011: Initial ice microparticle sublimation measurements from the levitating upper-tropospheric environmental simulator (LUTES). *J. Atmos. Ocean. Tech.*, **28**, 884– 890.

Miller, T., and K. Young, 1979: A numerical simulation of ice cyrstal growth from the vapor phase. *J. Atmos. Sci.*, **36**, 458–469.

Ming, N.-B., K. Tsukamoto, I. Sunagawa, and A. Chernov, 1988: Stacking faults as self-perpetuating step sources. *Journal of Crystal Growth*, **91**, 11–19.

Morrison, H., M. Witte, G. Bryan, J. Harrington, and Z. Lebo, 2018: Broadening of modeled cloud droplet spectra using bin microphysics in an eulerian spatial domain. *J. Atmos. Sci.*, **75**, 4005–4029.

Nelson, J., 1998: Sublimation of ice crystals. *J. Atmos. Sci.*, **55**, 910–919.

Nelson, J., 2001: Growth mechanisms to explain the primary and secondary habits pf snow crystals. *Philos. Mag. A.*, **81**, 2337–2373.

737 Nelson, J., 2005: Interactive comment on "supersaturation dehydration, and dentrification in arctic
738 cirrus" by B. Kacher. *Atmos. Chem. Phys. Discuss.*, **5**, S257–S260.

739 Nelson, J., and M. Baker, 1996: New theoretical framework for studies of vapor growth and
740 sublimation of small ice crystals in the atmosphere. *J. Geophys. Res.*, **101**, 7033–7047.

741 Nelson, J., and C. Knight, 1998: Snow crystal habit changes explained by layer nucleation. *J.*
742 *Atmos. Sci.*, **55**, 1452–1465.

743 Nelson, J., and B. Swanson, 2019: Air pockets and secondary habits in ice from lateral-
744 type growth. *Atmospheric Chemistry and Physics Discussions*, **2019**, 1–51, doi:10.5194/
745 acp-2019-280.

746 Neshyba, S., J. Adams, K. Reed, P. M. Rowe, and I. Gladich, 2016: A quasi-liquid mediated
747 continuum model of faceted ice dynamics. *Journal of Geophysical Research: Atmospheres*,
748 **121 (23)**, 14,035–14,055, doi:10.1002/2016JD025458.

749 Neshyba, S., B. Lowen, M. Benning, A. Lawson, and P. Rowe, 2013: Roughness metrics of
750 prismatic facets of ice. *J. Geophys. Res.*, **118**, 3309–3318, doi:10.1002/jgrd.50537.

751 Pardo, L., H. Morrison, L. Mchado, J. Harrington, and Z. Lebo, 2020: Drop size distribution
752 broadening mechanisms in a bin microphysics eulerian model. *J. Atmos. Sci.*, Early online re-
753 lease.

754 Pedersen, C., A. Mihranyan, and M. Stromme, 2011: Surface transition on ice induced by the
755 formation of a grain boundary. *PLoS ONE*, **6**, e24 373.

756 Pokrifka, G., A. Moyle, L. Hanson, and J. Harrington, 2020: Estimating surface attachment kinetic
757 and growth transition influences on vapor-grown ice crystals. *J. Atmos. Sci.*, **77**, 2393–2410.

Reisin, T., Z. Levin, and S. Tzivion, 1996: Rain production in convective clouds as simulated in an axisymmetric model with detailed microphysics. Part I: Description of the model. *J. Atmos. Sci.*, **53**, 497–519.

Saito, Y., 1996: *Statistics Physics of Crystal Growth*. World Scientific, 179pp.

Sheridan, L. M., J. Y. Harrington, D. Lamb, and K. Sulia, 2009: Influence of ice crystal aspect ratio on the evolution of ice size spectra during vapor depositional growth. *J. Atmos. Sci.*, **66**, 3732–3743.

Shima, S.-I., Y. Sato, A. Hashimoto, and R. Misumi, 2020: Predicting the morphology of ice particles in deep convection using the super-droplet method: development and evaluation of SCALE-SDM 0.2.5-2.2.0, -2.2.1, and -2.2.2. *Geosci. Model Dev.*, **13**, 4107–4157.

Sibley, D., P. Llombart, E. Noya, A. Archer, and L. MacDowell, 2021: How ice grows from premelting fims and water droplets. *Nature Communications*, **12**, 1–11.

Stevens, B., G. Feingold, W. R. Cotton, and R. L. Walko, 1996: Elements of the microphysical structure of numerically simulated nonprecipitating stratocumulus. *J. Atmos. Sci.*, **53**, 980–1007.

Strickland-Constable, R. F., 1968: *Kinetics and mechanism of crystallization from the fluid phase and of the condensation and evaporation of liquids*. Academic Press, London;New York;, 356 pp.

Sulia, K., and J. Harrington, 2011: Ice aspect ratio influences on mixed-phase clouds. Part I: Impacts on phase partitioning in parcel models. *J. Geophys. Res.*, **116**, doi:10.1029/2011JD016298.

Thompson, G., P. Field, R. Rasmussen, and W. Hall, 2008: Explicit forecasts of winter precipitation using an improved bulk microphysics scheme. Part II: Implementation of a new snow parameterization. *Mon. Wea. Rev.*, **136**, 5095–5115, doi:10.1175/2008MWR2387.1.

Todd, C. J., 1964: A system for computing ice phase hydrometeor development. Rept. arg-64 pa-121, pp. 30., Meteorology Research Inc.

Tzivion, S., G. Feingold, and Z. Levin, 1989: The evolution of rain-drop spectra. part ii: Collisional collection/breakup and evaporation in a rain shaft. *J. Atmos. Sci.*, **46**, 3312–3327.

Wood, S., M. Baker, and D. Calhoun, 2001: New model for the vapor growth of hexagonal ice crystals in the atmosphere. *J. Geophys. Res.*, **106**, 4845–4870.

Wu, T., 1999: Numerical modeling of the November 26, 1991 cirrus event. Ph.D. thesis, Colorado State University.

Zhang, C., 2012: A unified theory for ice vapor growth suitable for cloud models: Testing and implications for cold cloud evolution. Ph.D. thesis, The Pennsylvania State University.

Zhang, C., and J. Harrington, 2014: Including surface kinetic effects in simple models of ice vapor diffusion. *J. Atmos. Sci.*, **71**, 372–390.

Zhang, C., and J. Harrington, 2015: The effects of surface kinetics on crystal growth and homogeneous freezing in parcel simulations of cirrus. *J. Atmos. Sci.*, **72**, 2929–2946.

LIST OF FIGURES

889 **Fig. 12.** Simulation and distribution averages of (a) the ice water content, (b) the effective density, (c)
890 the a-axis semi-length and, (d) the c-axis semi-length as a function of the initial temperature
891 of the simulation. Initial ice crystal concentrations of 10 (black lines), 50 (red lines), and 500
892 (blue lines) L^{-1}, along with a constant updraft speed of 0.25 m s^{-1} and an initial pressure of
893 850 hPa were used. Ice crystal growth assumed step nucleation ($M = 10$). Results from the
894 Lagrangian bin (solid), Eulerian bin (dashed), and bulk (circle-dashed) models are shown. . . 51

895 **Fig. 13.** Simulation and distribution average of (a) the a-axis (black) and c-axis (red) semi-lengths,
896 and (b) the mass-weighted fall speed as a function of the initial temperature. An initial
897 ice concentration of 10 L^{-1}, along with a constant updraft speed of 0.25 m s^{-1} and an
898 initial pressure of 850 hPa were used. Ice crystal growth assumed step nucleation ($M = 10$).
899 Lagrangian and bulk model results are shown by the solid line and the dashed-dotted lines,
900 respectively. Eulerian bin model results are shown by the red dashed line for the fall speed
901 only. The influence of the assumed distribution shape on the axis lengths is indicated by
902 the long-dashed and short-dashed lines bounding the shaded regions. The bounding long-
903 dashed and short dashed lines used a distribution shape of $\nu = 3$ and $\nu = 6$, respectively. For
904 reference, this is indicated for the c-axis in (a). 52

905 **Fig. 14.** Simulation and distribution average of the (a) ice water content growth rate and (b) the
906 deposition coefficients as a function of the initial temperature. Results are shown for bulk
907 model simulations using both deposition coefficients ($\overline{\alpha}_a$ and $\overline{\alpha}_c$, solid lines) and bulk model
908 simulations using a single deposition coefficient as could be used in classical bulk models
909 (dashed-dotted lines). The ice water content growth rate is shown three initial ice concen-
910 trations of 10 (black lines), 50 (red lines), and 500 (blue lines) L^{-1}, along with a constant
911 updraft speed of 0.25 m s^{-1} and an initial pressure of 850 hPa. The deposition coefficients
912 are shown only for the simulation with an ice concentrations of 10 L^{-1}. 53

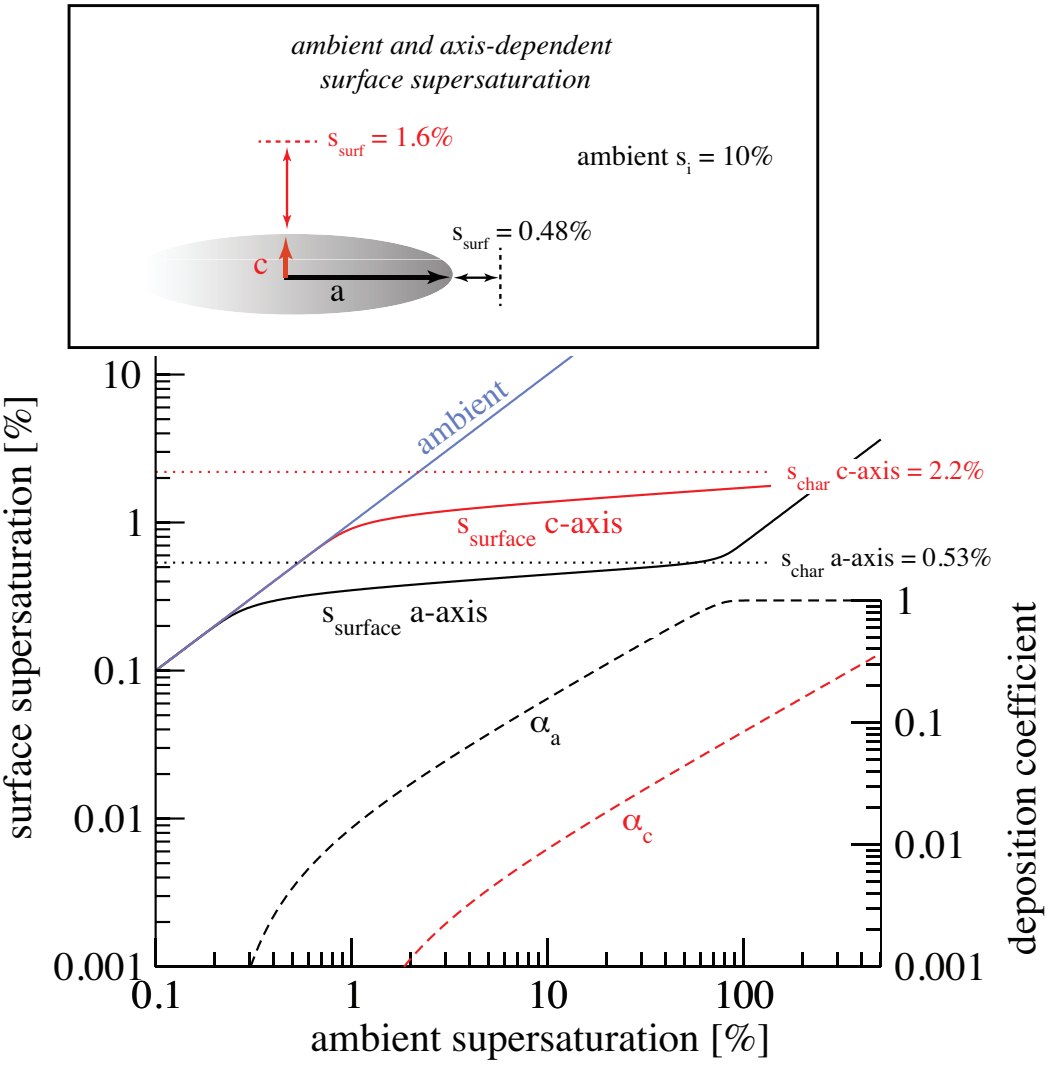

FIG. 1. Variation of the surface supersaturations (left axis, solid lines) and the deposition coefficients (right axis, dashed lines) as a function of the ambient supersaturation for a crystal with an *a*-axis of 86 μm, a *c*-axis of 17 μm, and at T = -15°C, P = 500 hPa. The one-to-one ambient supersaturation line is shown on the figure in blue and is labeled. The surface supersaturation and deposition coefficient for the *a* and *c* axes are given by the black and red curves (respectively) and are labeled on the figure. The characteristic supersaturation for each axis is indicated by the dotted lines with c-axis s_{char} = 2.2% (red) and a-axis s_{char} = 0.53% (black). The cartoon at the top illustrates the surface supersaturation for each axis (dashed line) at an ambient supersaturation of 10%. The proximity of the dashed line to the surface indicates the degree of supersaturation (s_{surf}).

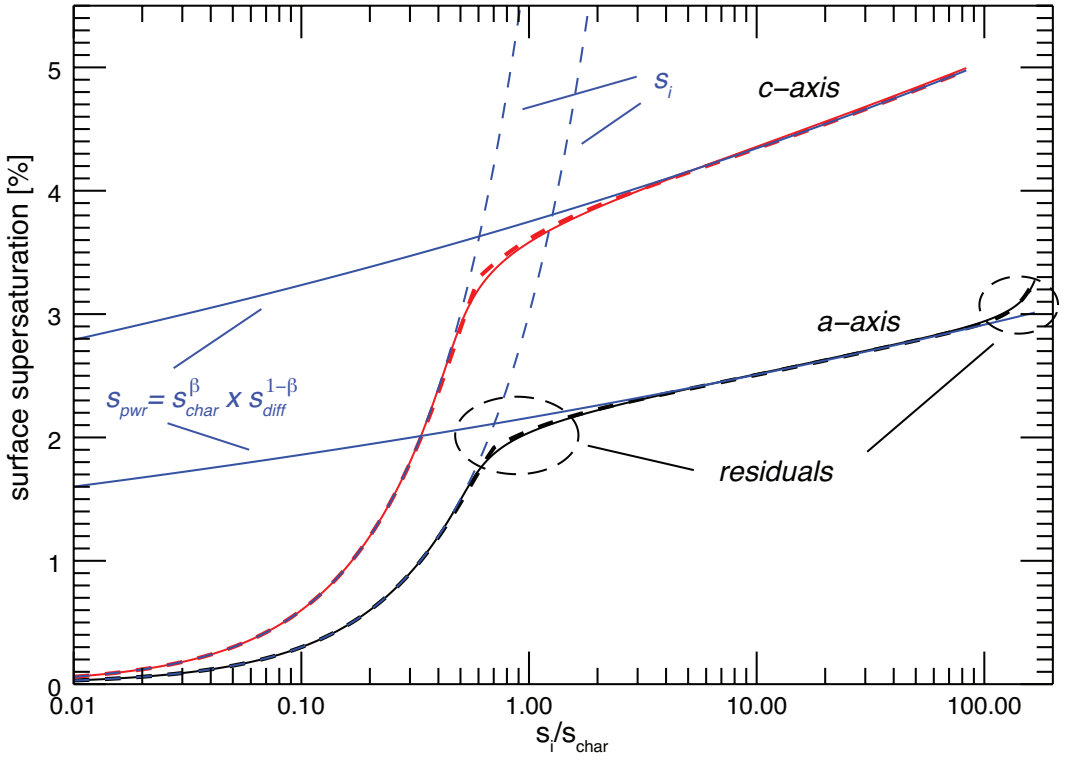

FIG. 2. Surface supersaturation as a function of the ratio of the ambient supersaturation to the characteristic value (s_i/s_{char}) for a planar crystal with an a-axis length of 240 μm, an aspect ratio of 0.1, a temperature of -35°C, and a pressure of 500 hPa. Ledge nucleation ($M = 10$) was assumed with characteristic supersaturations for the a- and c-axes of s_a = 3% and s_c = 6%, respectively. Exact calculation of s_{sfc} for the a- and c-axes are shown with the solid black and red lines, respectively whereas the parameterization is shown with the dashed lines. The ambient supersaturation is indicted by the blue dashed lines, and the power-law fit (s_{pwr}) is given by the solid blue lines for each axis. Deviations from the power-law fit are indicated by the black circles and labeled residuals, using the a-axis as an example.

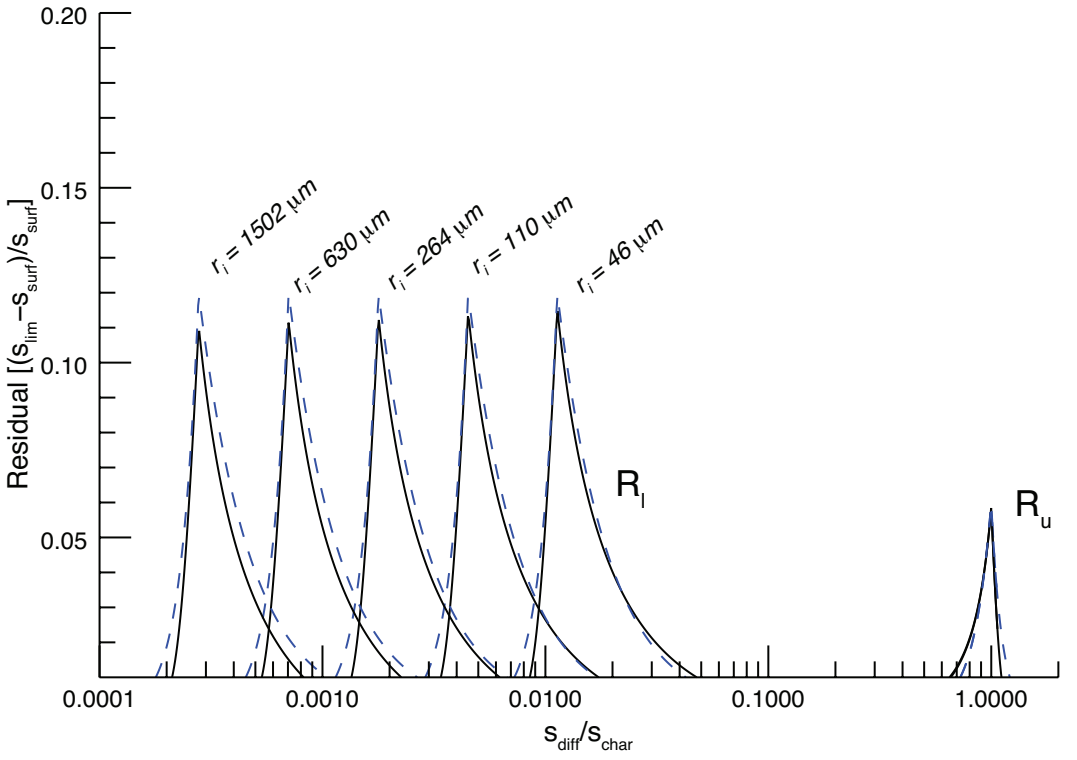

FIG. 3. Residuals (black lines) as a function of s_{diff}/s_{char} computed from the difference between the limited power-law value (s_{lim}) and the actual surface supersaturation (s_{surf}). The residuals are given as a fractional quantity. The temperature, pressure, growth mechanism, and aspect ratio were the same as Fig. 2. The particle size was varied by keeping the aspect ratio constant and changing the radius of an equivalent volume sphere (r_{eq}). The dashed blue lines show the parameterized residuals: R_l varies implicitly with size whereas R_u is fixed near unity.

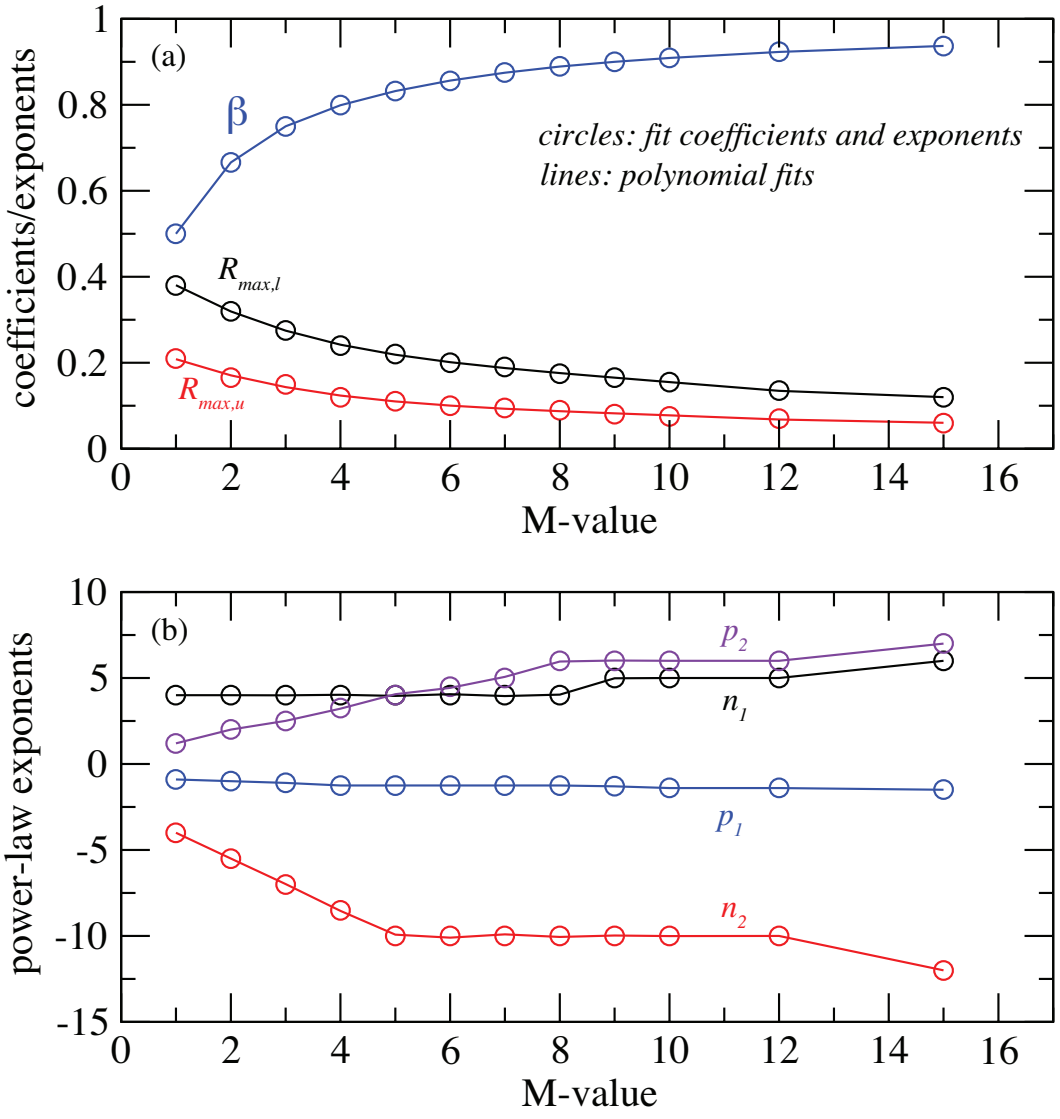

935 FIG. 4. Deposition coefficient growth mechanism parameter M-dependence of, (a) power-law exponent used
936 in Eq. 6 and coefficients used in Eq. 9, and (b) power-law exponents used in Eq. 9. Circles represent the actual
937 values used to fit Eqs. 6 and 9 to accurate calculations of the surface supersaturation (values are given in Table
938 1). Lines are polynomial fits to the circles, and the fit coefficients are given in Table 2.

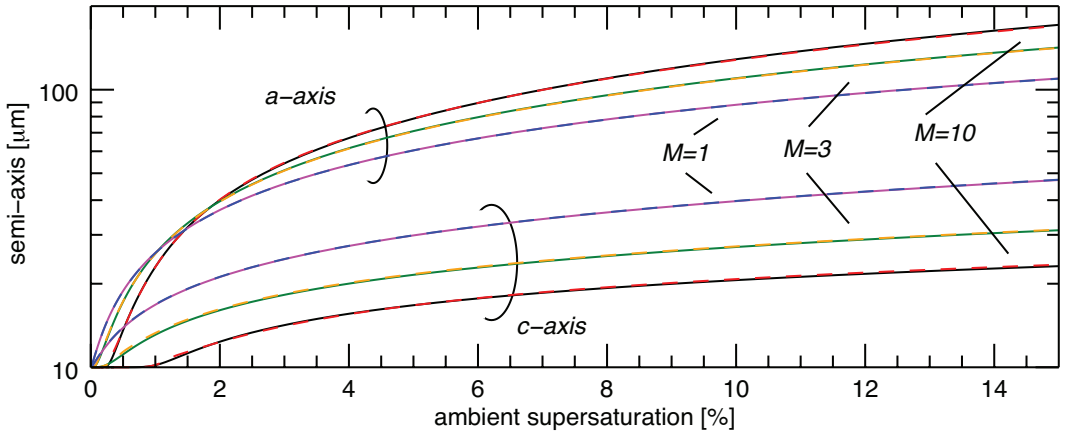

939 FIG. 5. Semi-axis lengths (a and c) after 10 minutes of growth at a pressure of 500 hPa and a temperature of
940 -15°C and a constant ambient supersaturation. Calculations are shown for three values of the growth mechanism
941 parameter, M, of 1 (dislocation growth), 3, and 10 (ledge formation), which are indicated by the lines. Bench-
942 mark calculations for three values M, are indicated by the magenta (M=1), green (M=3), and black (M=10) lines.
943 Simulations using the approximate form of the deposition coefficient are indicated by the dashed blue (M=1),
944 orange (M=3), and red (M=10) lines.

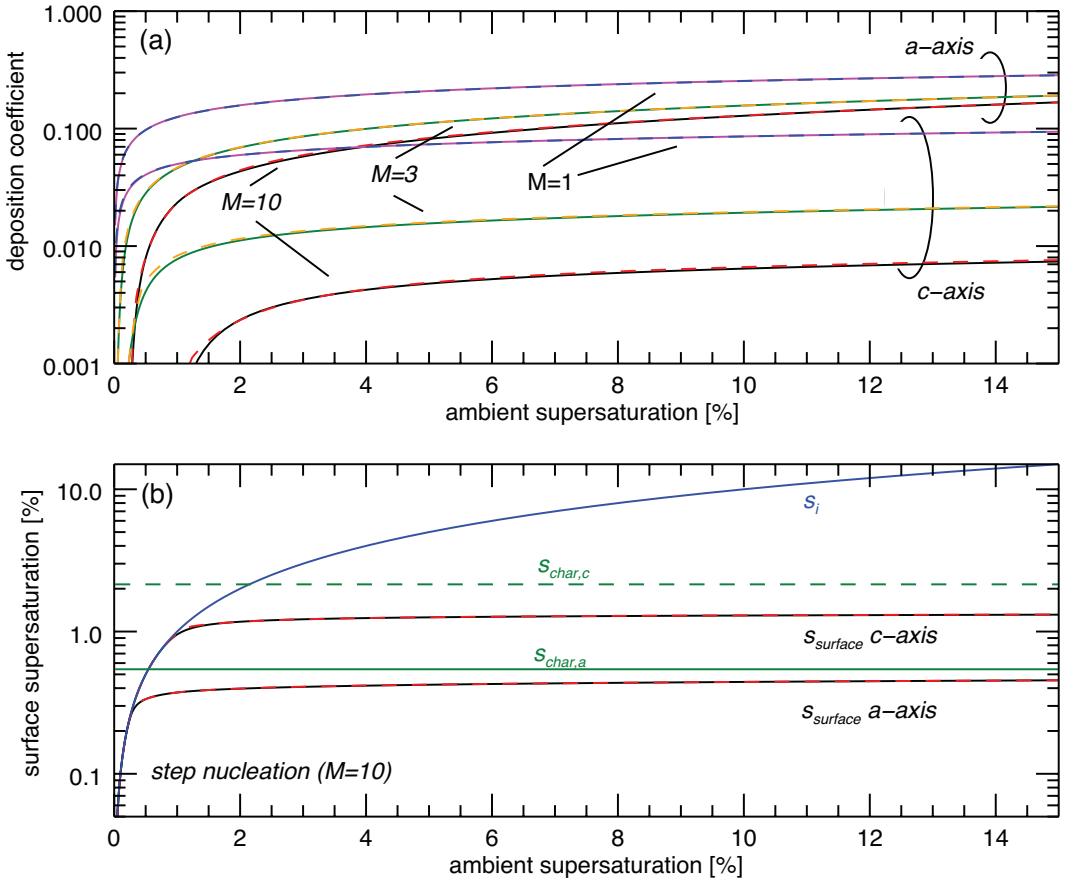

FIG. 6. (a) Deposition coefficients (a and c) after 10 minutes of growth at a pressure of 500 hPa, a temperature of -15°C as a function of the ambient supersaturation (s_i). Calculations are shown for three values of the growth mechanism parameter, M, of 1 (dislocation growth), 3, and 10 (ledge formation), which are indicated by the curves. Benchmark calculations for three values M, are indicated by the magenta (M=1), green (M=3), and black (M=10) curves. Simulations using the approximate form of α are indicated by the dashed blue (M=1), orange (M=3), and red (M=10) curves. (b) Surface supersaturation for the a- and c-axes as a function of s_i for step nucleation (M = 10). Benchmark calculations are shown with the black curve, whereas the approximate form is given by the red-dashed curve. The one-to-one ambient supersaturation is given by the blue curve, and the values of s_{char} for the a- and c-axes are given by the green solid and dashed lines, respectively.

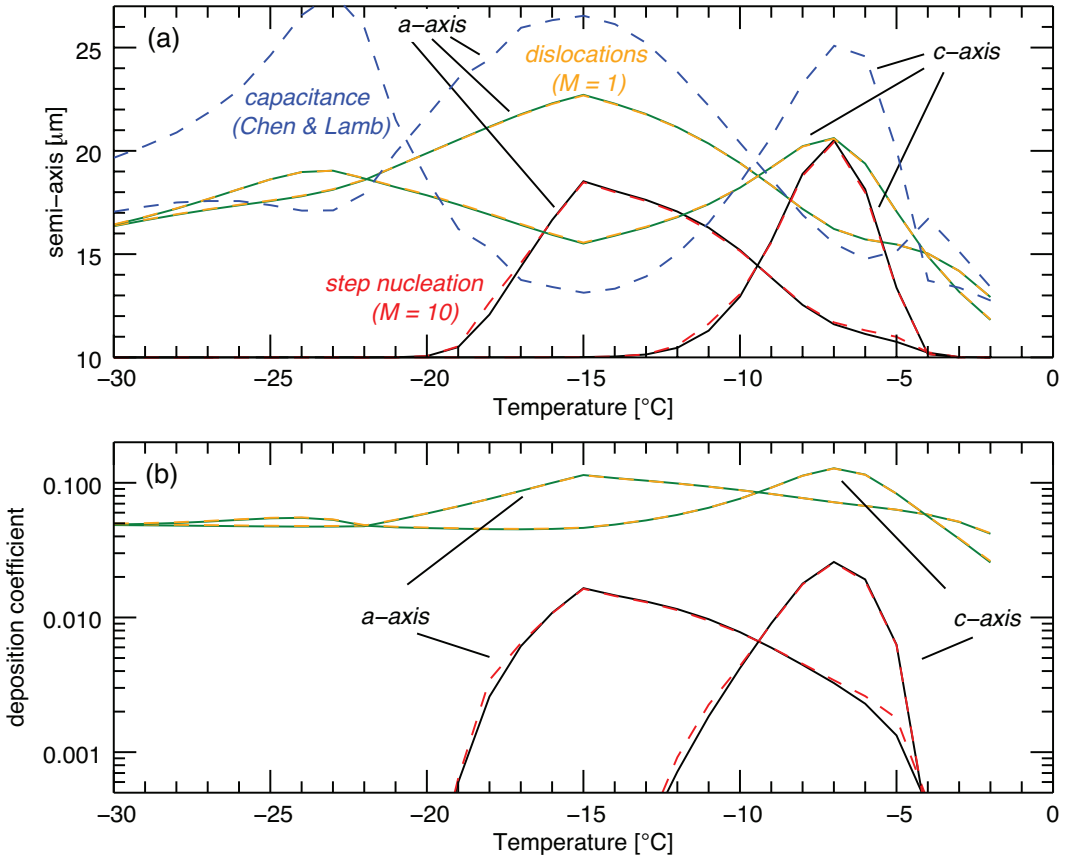

954 FIG. 7. (a) Semi-axis lengths (a and c) and, (b) deposition coefficients after 10 minutes of growth at a pressure
955 of 500 hPa, a temperature of -15°C, an initial crystal radius of 10μm, and a constant ambient supersaturation
956 that is 5% of liquid saturation, $s_i = 0.05 \times [e_s - e_i]/e_i$ where e_s and e_i are the equilibrium vapor pressures of
957 liquid and ice, respectively. Accurate benchmark calculations are indicated by the green (M=1, dislocations),
958 and black (M=10, step nucleation) lines. Simulations using the approximate form of the deposition coefficient
959 are indicated by the dashed orange (M=1) and dashed red (M=10) lines. Simulations using the capacitance
960 model with the Chen and Lamb (1994) habit parameterization is shown by the blue dashed lines.

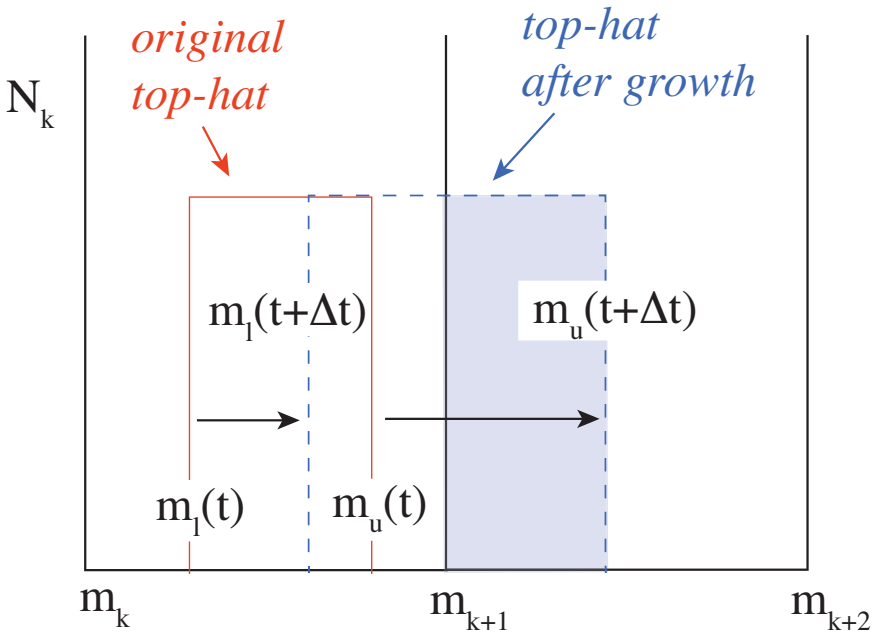

961 FIG. 8. Cartoon example of top-hat semi-Lagrangian depositional growth (Stevens et al. 1996). Bin mass
962 edges are given along the x-axis as m_k and m_{k+1} defining bin-k. The edges of the original top-hat construction in
963 bin-k is shown in red, with the lower and upper mass edges shown ($m_l(t)$ and $m_u(t)$, respectively). The analytical
964 solution to the vapor growth equation is used to calculate the change in the top-hat edges indicated by the black
965 arrows ($m_l(t+\Delta t)$ and $m_u(t+\Delta)$), resulting in a new top-hat distribution shown by the dashed blue lines. In
966 this example, the number mixing ratio (N_k) is then remapped to the next bin ($k+1$) using the fraction shown
967 by the blue shade, while the remainder (shown in white) is mapped to the original bin. The total concentration
968 (zeroth-moment) is conserved in this process. This procedure is used to remap the mass, volume, and aspect
969 ratio.

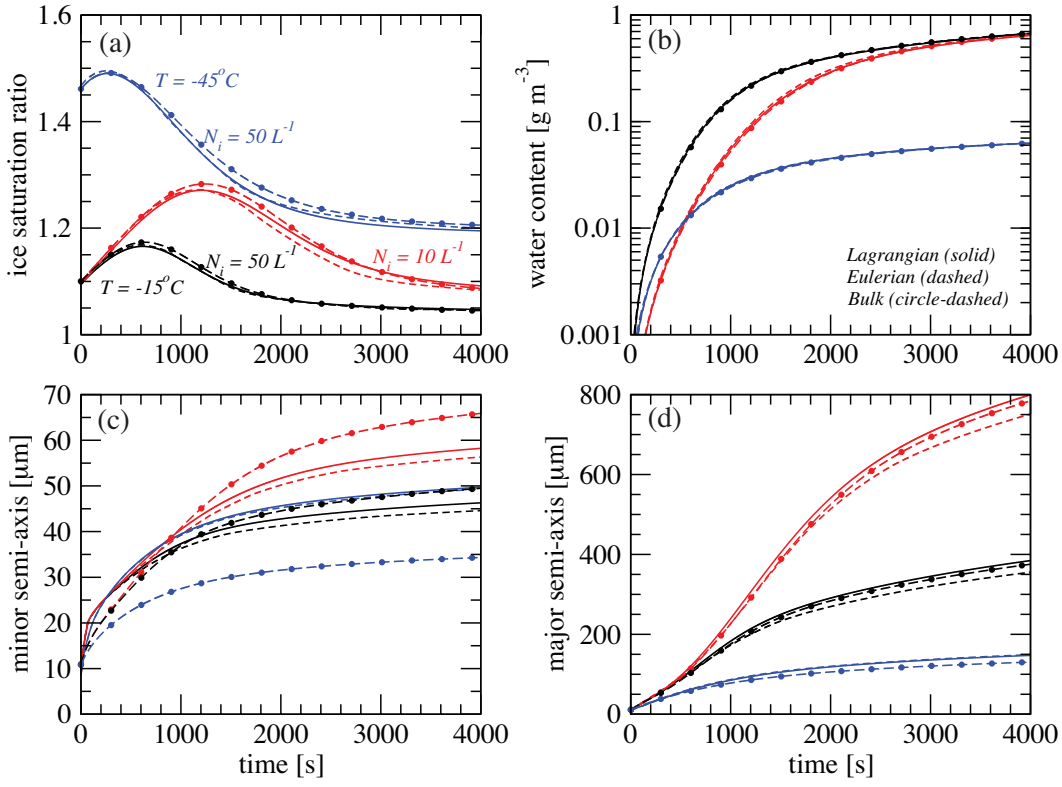

970 FIG. 9. Parcel model simulation time-series of (a) ice saturation ratio (e/e_i), (b) ice water content, (c) minor
971 semi-axis length, and (d) major semi-axis length. The simulations were conducted for two different initial tem-
972 peratures (-15°C, red and black, and -45°C, blue) and two difference ice concentrations for the -15°C simulation
973 (labeled on panel a). Both simulations used a constant updraft speed of 0.25 m s^{-1}. An initial pressure of 850
974 hPa (300 hPa) was assumed for the -15°C (-45°C) simulation. Note that the major axis at -15°C (-45°C) is the
975 a-axis (c-axis). Ice crystal growth assumed step nucleation ($M = 10$). Results using the Lagrangian bin (solid),
976 Eulerian bin (dashed), and bulk (circle-dashed) models are shown.

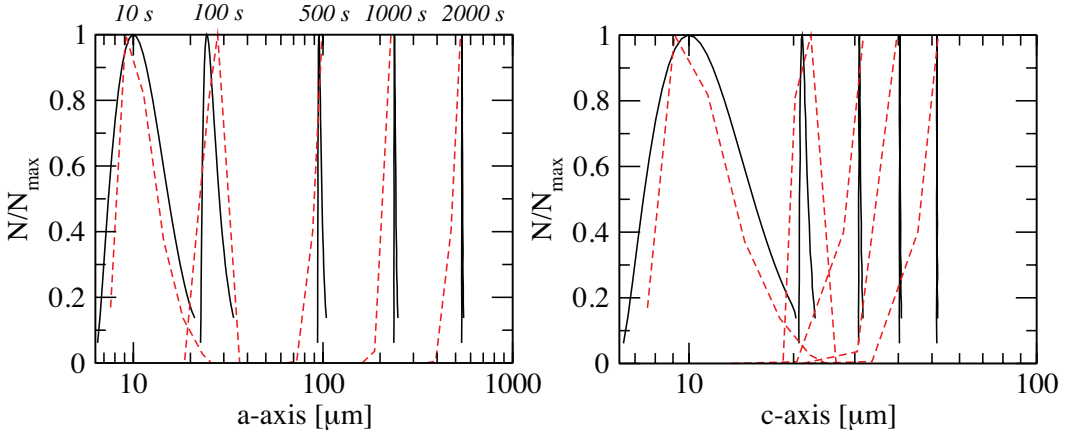

977 FIG. 10. Distributions of fractional ice concentration (N/N_{max}) as a function of the a-axis (left panel) and
978 c-axis (right panel) semi-lengths. N is the ice crystal concentration and N_{max} is the concentration at the distri-
979 bution peak (mode). Lagrangian microphysical model distributions are given by the solid lines, Eulerian bin
980 microphysical distributions by the dashed red lines. Distributions are plotted at the simulation times indicated
981 above the distributions shown in the left panel. Distributions are plotted for the simulation with an initial tem-
982 perature of -15°C, an initial pressure of 850 hPa, an ice concentration of 10 L^{-1}, and a constant updraft speed of
983 0.25 m s^{-1}.

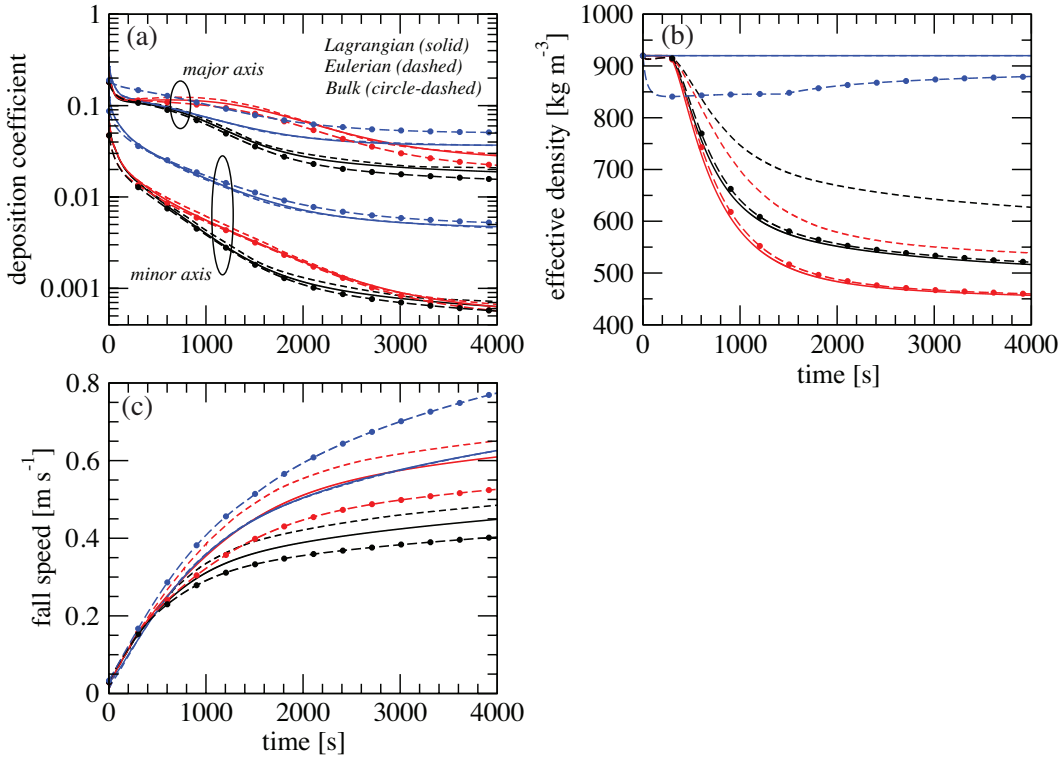

984 FIG. 11. Parcel model simulation time-series of average (a) deposition coefficients for the minor and major
985 semi-axes (b) effective particle density, and (c) mass-weighted fall speed. The simulations were conducted for
986 two different initial temperatures (-15°C, red and black, and -45°C, blue) and two difference ice concentrations
987 for the -15°C simulation (labeled on panel a). Both simulations used a constant updraft speed of 0.25 m s^{-1}.
988 An initial pressure of 850 hPa (300 hPa) was assumed for the -15°C (-45°C) simulation. Note that the major
989 axis at -15°C (-45°C) is the a-axis (c-axis). Ice crystal growth assumed step nucleation ($M = 10$). Results using
990 the Lagrangian bin (solid), Eulerian bin (dashed), and bulk (circle-dashed) models are shown.

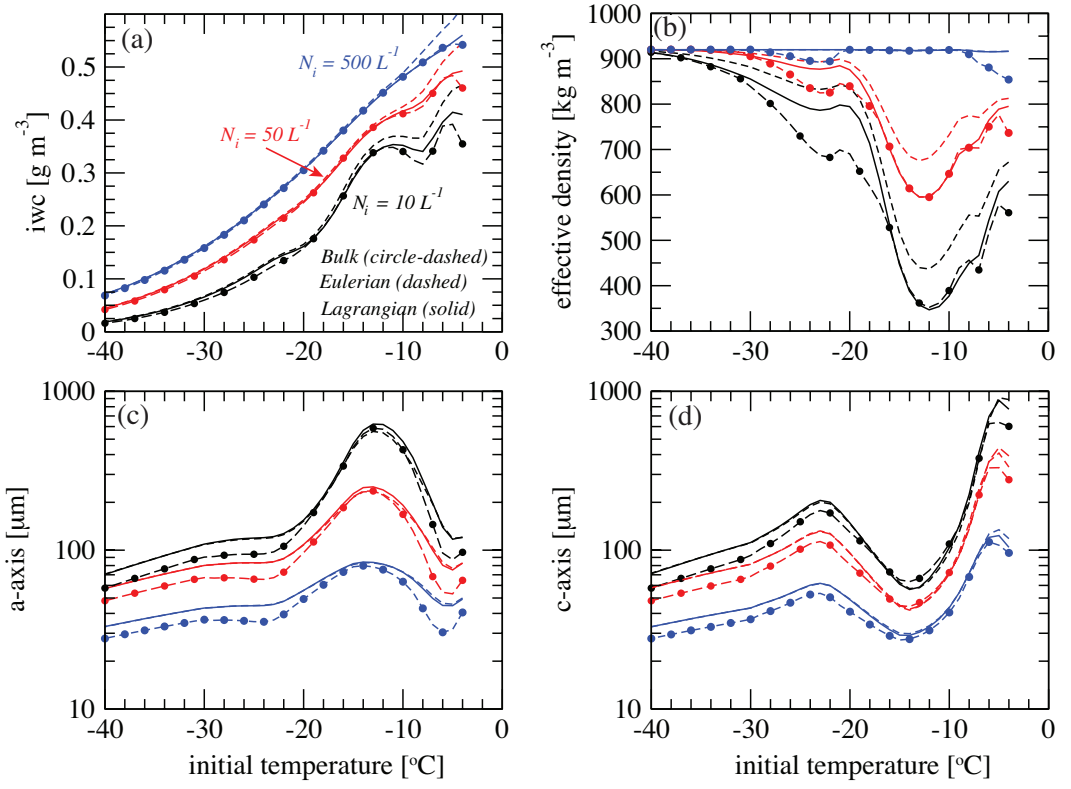

FIG. 12. Simulation and distribution averages of (a) the ice water content, (b) the effective density, (c) the a-axis semi-length and, (d) the c-axis semi-length as a function of the initial temperature of the simulation. Initial ice crystal concentrations of 10 (black lines), 50 (red lines), and 500 (blue lines) L^{-1}, along with a constant updraft speed of 0.25 m s^{-1} and an initial pressure of 850 hPa were used. Ice crystal growth assumed step nucleation ($M = 10$). Results from the Lagrangian bin (solid), Eulerian bin (dashed), and bulk (circle-dashed) models are shown.

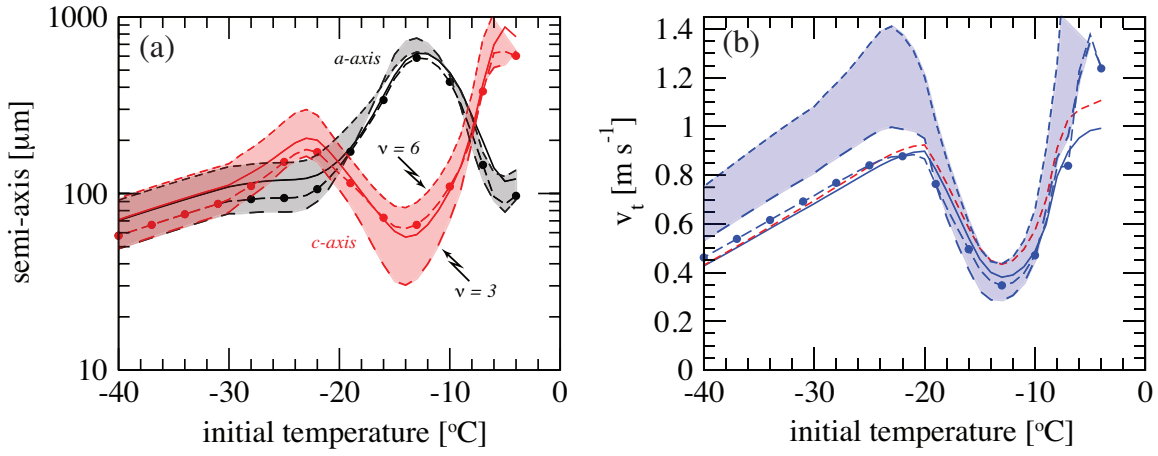

FIG. 13. Simulation and distribution average of (a) the a-axis (black) and c-axis (red) semi-lengths, and (b) the mass-weighted fall speed as a function of the initial temperature. An initial ice concentration of 10 L^{-1}, along with a constant updraft speed of 0.25 m s^{-1} and an initial pressure of 850 hPa were used. Ice crystal growth assumed step nucleation ($M = 10$). Lagrangian and bulk model results are shown by the solid line and the dashed-dotted lines, respectively. Eulerian bin model results are shown by the red dashed line for the fall speed only. The influence of the assumed distribution shape on the axis lengths is indicated by the long-dashed and short-dashed lines bounding the shaded regions. The bounding long-dashed and short dashed lines used a distribution shape of $\nu = 3$ and $\nu = 6$, respectively. For reference, this is indicated for the c-axis in (a).

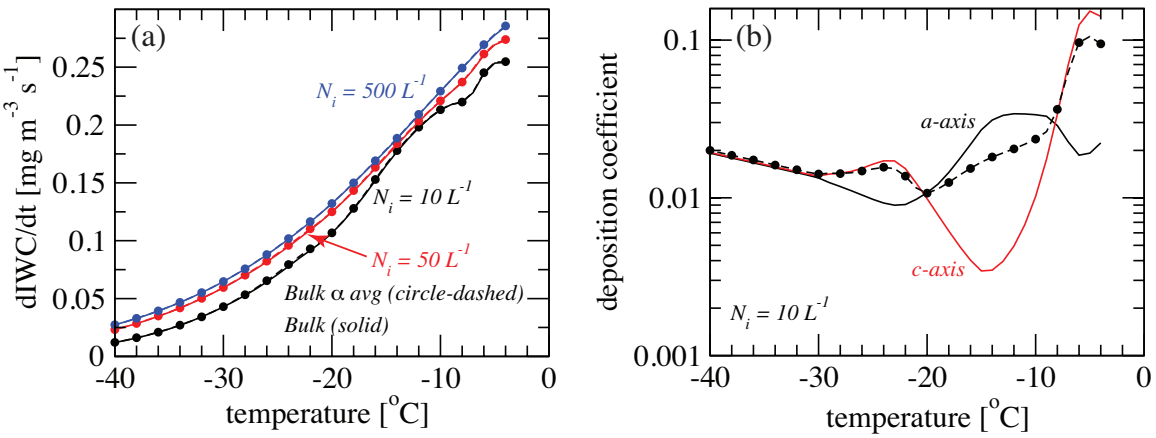

FIG. 14. Simulation and distribution average of the (a) ice water content growth rate and (b) the deposition coefficients as a function of the initial temperature. Results are shown for bulk model simulations using both deposition coefficients ($\overline{\alpha}_a$ and $\overline{\alpha}_c$, solid lines) and bulk model simulations using a single deposition coefficient as could be used in classical bulk models (dashed-dotted lines). The ice water content growth rate is shown three initial ice concentrations of 10 (black lines), 50 (red lines), and 500 (blue lines) L^{-1}, along with a constant updraft speed of 0.25 m s^{-1} and an initial pressure of 850 hPa. The deposition coefficients are shown only for the simulation with an ice concentrations of 10 L^{-1}.